

Photosphere emission from a hybrid relativistic outflow with arbitrary dimensionless entropy and magnetization in GRBs

He Gao¹, Bing Zhang

Department of Physics and Astronomy, University of Nevada Las Vegas, NV 89154, USA
gaohe@physics.unlv.edu; zhang@physics.unlv.edu

ABSTRACT

The composition of gamma-ray burst (GRB) ejecta is still a mystery, which stimulated an intense debate about the physical origin of GRB prompt emission. Recent broad-band observations of GRBs with the *Fermi* satellite call for a “hybrid” central engine, with both a hot “fireball” component and a cold “Poynting flux” component. In this paper, we develop a theory of photosphere emission from such a hybrid relativistic outflow with an arbitrary dimensionless entropy η and magnetization σ_0 at the central engine. We develop two approaches: a “bottom-up” approach to predict the temperature and luminosity of the photosphere emission and its relative brightness with respect to the non-thermal emission component from an optically thin region, for a given pair of (η, σ_0) ; and a “top-down” approach to diagnose central engine parameters (η and σ_0) based on the observed photosphere emission properties. For both approaches, we consider two possibilities: one is that the Poynting flux does not suffer significant dissipation beneath the photosphere, while the other is that there is such dissipation. From our bottom-up approach, we show that a variety of observed GRB prompt emission spectra with different degrees of photosphere emission can be reproduced by varying η and σ_0 . In order to reproduce the observed spectra, the outflows of most GRBs need to have a significant σ , both at the central engine, and at the photosphere. The σ value at 10^{15} cm from the central engine (a possible non-thermal emission site) is usually also greater than unity, so that internal-collision-induced magnetic reconnection and turbulence (ICMART) may be the mechanism to power the non-thermal emission. We apply our top-down approach to the time-resolved spectral data of GRB 110721A, and diagnose its time-dependent central engine parameters. We find that the temporal behavior of the blackbody component in its time-resolved spectrum can be well interpreted

¹Current address: Department of Astronomy and Astrophysics, Department of Physics, Center for Particle Astrophysics, The Pennsylvania State University, University Park, PA 16802, USA; hug18@psu.edu

with a time-varying (η, σ_0) at the central engine, instead of invoking a varying engine base size r_0 as proposed by previous authors. Future systematic studies of GRB spectra using our method would lead to diagnostics of jet composition of many GRBs, shedding light to the GRB prompt emission mechanism.

1. Introduction

After decades of investigations, the origin of gamma-ray burst (GRB) prompt emission is still poorly understood. The main obstacle in front of theorists is one fundamental question: *What is the composition of GRB jets?*

In the early picture discussed by Paczynski (1986) and Goodman (1986), GRB outflows originate from an initially hot “fireball” composed of photons and electron/positron pairs. The emergent spectrum from the fireball photosphere is a modified blackbody, which is inconsistent with the typical observed spectrum, characterized by a smoothly-joint broken power-law function known as the “Band” function (Band et al. 1993). Observationally, the typical low- and high-energy photon indices of the Band function are distributed around $\alpha \sim -1$ and $\beta \sim -2.2$, respectively (Preece et al. 2000), which disfavor a simplest fireball photosphere model. Shemi & Piran (1990) showed that when a small amount of baryons are added to the fireball, a significant fraction of the initial fireball thermal energy is converted to the kinetic energy of the outflow, after an initially rapid acceleration phase under fireball’s thermal pressure (Mészáros et al. 1993; Piran et al. 1993). In order to produce non-thermal photons, the kinetic energy of the outflow needs to be dissipated, either in the external shock (Rees & Mészáros 1992; Mészáros & Rees 1993) or internal shocks (hereafter IS, Rees & Mészáros 1994). Synchrotron (and possibly also synchrotron self-Compton) radiation by the relativistic electrons accelerated in these shocks give rise to the observed non-thermal γ -ray emission (Mészáros et al. 1994; Tavani 1996; Daigne & Mochkovitch 1998; Lloyd & Petrosian 2000). Within such a “fireball shock” model, the observed spectrum is expected to be the superposition of two components: a non-thermal component from the IS in the optically thin region, and a quasi-thermal component from the fireball photosphere (Mészáros & Rees 2000; Mészáros et al. 2002; Pe’er et al. 2006).

Before *Fermi*, it has been claimed that the spectra of some BATSE GRBs can be fit with the superposition of a blackbody component and an underlying power law (e.g. Ghirlanda et al. 2002, 2003; Ryde 2005; Ryde & Pe’er 2009). Due to the narrowness of the energy band, one was not able to exclude other models, so as to firmly establish the thermal model. Most BATSE GRBs, on the other hand, have a dominant Band function component for both time-integrated and time-resolved spectra. There are several competing models

to interpret the peak energy E_p in the pre-*Fermi* era (Zhang & Mészáros 2002). If it is the synchrotron peak from the IS, then the absence of the photospheric emission component would imply that GRB jets are magnetically dominated (Daigne & Mochkovitch 2002; Zhang & Mészáros 2002). Within this scenario, the GRB radiation is powered by dissipation of the magnetic field energy in the ejecta (Usov 1994; Thompson 1994; Mészáros & Rees 1997; Lyutikov & Blandford 2003). Alternatively, the Band function itself may be emission from a dissipative photosphere (Rees & Mészáros 2005; Giannios 2008; Beloborodov 2010; Ioka 2010; Lazzati & Begelman 2010; Pe’er & Ryde 2011; Vurm et al. 2011; Giannios 2012; Lundman et al. 2013).

Having both Gamma-ray Burst Monitor (GBM, Meegan et al. 2009) and Large Area Telescope (LAT, Atwood et al. 2009) on board, *Fermi* opened the spectral window to cover 6-7 orders of magnitude in energy, allowing a close investigation of various spectral components in the GRB prompt emission spectra. The first bright LAT GRB, GRB 080916C, showed nearly featureless Band spectra in 5 different time bins over 6-7 orders of magnitude in energy (Abdo et al. 2009a; Zhang et al. 2011). Assuming the standard fireball shock model and using parameters derived from the observational data, Zhang & Pe’er (2009) showed that a quasi-thermal photosphere component would greatly outshine the non-thermal component if GRB 080916C is a fireball. The non-detection of such a bright photosphere component allowed Zhang & Pe’er (2009) to claim that the jet of GRB 080916C is Poynting-flux-dominated, and a lower limit of σ was set at the photosphere¹. In order to interpret the non-thermal emission in a Poynting flux dominated outflow, Zhang & Yan (2011) proposed an “internal-collision-induced magnetic reconnection and turbulence” (ICMART) model for GRBs.

The quasi-thermal component predicted by the fireball model was later observed in some *Fermi* GRBs. GRB 090902B (Abdo et al. 2009b) is the most prominent one, which shows a narrow Band function component superposed on an underlying power law component in the time integrated spectrum. When a time-resolved spectral analysis was carried out, a multi-color blackbody (Ryde et al. 2010) or even a blackbody (Zhang et al. 2011) component was revealed. This component is well interpreted as photosphere emission from a fireball (Pe’er et al. 2012). Later, several more GRBs have a thermal spectral component identified in the time-integrated and time-resolved spectra, but the component is sub-dominant (e.g. GRB 100724B, Guiriec et al. 2011; GRB 110721A Axelsson et al. 2012; and the short GRB

¹A recent more detailed investigation (S. Guiriec et al. 2014, in preparation) revealed a weak photosphere component in GRB 080916C. Its peak flux is roughly at the flux level that Zhang & Pe’er (2009) used to derive the lower limit of σ . As a result, the conclusion of Zhang & Pe’er (2009) that GRB 080916C is a Poynting flux dominated remains valid, with the derived lower limit of σ replaced by the real value of σ .

120323A Guiriec et al. 2013). Since these thermal components are superposed on a Band component, it suggests that the Band emission component is not the modified thermal emission from the photosphere². Rather, the Band component likely originates from an optically thin region, e.g. the IS or the ICMART site. The fact that GRB 110721A has a 15-MeV E_p at early epochs strongly disfavors the photosphere origin of the Band component, since it exceeds the maximum temperature a photosphere can reach for the observed luminosity (Zhang et al. 2012, see also Veres et al. 2012).

The available data suggest that the photosphere emission in GRBs has diverse properties. While in rare cases (e.g. GRB 090902B) it can be the dominant emission component, in many more cases, it is either a sub-dominant component, or non-detectable. A plausible interpretation (e.g. Zhang 2011) would be that GRBs have a diverse jet composition. While some are more matter-dominated (which resemble traditional fireballs), many others have more magnetized ejecta with a range of magnetization degree (σ) at the central engine, the photosphere, and the non-thermal emission site. Two key parameters are the dimensionless entropy η and magnetization σ_0 at the central engine. If η is large and $\sigma_0 \ll 1$, one gets a hot fireball with a dominant photosphere component (e.g. in GRB 090902B). If η is smaller while σ_0 is larger, the thermal emission is suppressed, so that the photosphere emission component is sub-dominant (e.g. in GRB 110721A). Finally, if η is close to unity while σ_0 is extremely large, the photosphere component is completely suppressed. This is an attractive possibility. However, so far no theory of photosphere emission of such a hybrid outflow has been developed in detail.

Within the framework of the fireball shock model, Pe’er et al. (2007) proposed a method to infer central engine parameters using observed data. With the measured temperature and flux of an identified thermal component in the spectrum, along with a flux ratio between thermal and non-thermal components, one may infer the size of the jet at the base of the outflow, r_0 , and the dimensionless entropy of the outflow, $\eta = L_w/\dot{M}c^2$ (which is also the bulk Lorentz factor of the outflow, if the photosphere radius is greater than the fireball coasting radius). Some authors have applied this method to some *Fermi* GRBs (Iyyani et al. 2013; Preece et al. 2014; Ghirlanda et al. 2013). The derived central engine parameters are sometimes ad hoc or inconsistent. For instance, the analyses for GRB 110721A (Iyyani et al. 2013) and for GRB 130427A (Preece et al. 2014) led to a curious conclusion that the bulk Lorentz factor of the outflow of different layers are decreasing with time. This would lead to no, or at most very inefficient, internal shock emission. Yet both bursts have dominant

²The photosphere model suffers from the difficulty to account for the low-energy photon index of the Band function, and may not account for the observed hard-to-soft E_p evolution pattern as observed in many GRBs (Deng & Zhang 2014).

non-thermal emission. More curiously, the data of GRB 110721A (Iyyani et al. 2013) require that r_0 is rapidly varying with time by 2-3 orders of magnitudes. This is hard to imagine given the well believed paradigm of GRB central engine: If the engine is naked, the size of the engine (a hyper-accreting black hole or a millisecond magnetar) is around $r_0 \sim 10^7$ cm; if an extended envelope of a collapsar progenitor is considered, the fireball may be “re-born”, with $r_0 \sim R_*\theta_j \sim 10^9 R_{*,10}\theta_{j,-1}$ cm (where R_* is the size of the progenitor star, and θ_j is the jet opening angle). If one considers the depletion of the envelope, r_0 should decrease with time. However, Iyyani et al. (2013) showed that r_0 increases from 10^6 cm to 10^8 cm early on, and then decreases mildly after 2 seconds. These absurd conclusions suggest that the starting point of the analysis, i.e. the assumption of a pure fireball model, might not be valid. It is interesting to see whether a hybrid ejecta photosphere model may solve the problem. Incidentally, Ghirlanda et al. (2013) analyzed another burst GRB 100507 using the fireball framework (Pe’er et al. 2007), but found that the derived r_0 remains constant and reasonable. The jet composition of that burst may be more close to a fireball. It would be interesting to see whether a general theoretical framework can be established, which may be reduced to the standard fireball framework when $\sigma_0 < 1$.

In this paper, we develop a theory of photosphere emission from a hybrid relativistic outflow with an arbitrary dimensionless entropy η and magnetization σ_0 at the central engine. In section 2, we describe the set-up of the problem, and introduce an approximate analytical description of the dynamical evolution of the hybrid system. In section 3, we develop a “bottom-up” approach by deriving the photosphere properties for given input parameters of the central engine. We then reverse the problem and develop a “top-down” approach in section 4, aiming at diagnosing the central engine parameters based on the observational data of the thermal emission component as well as its relative brightness with respect to the non-thermal component. In section 5, we apply this method to GRB 110721A and derive its central engine parameters as well as their temporal evolution. Throughout the paper, the convention $Q = 10^n Q_n$ is adopted for cgs units.

2. Hybrid system and its dynamical evolution

The acceleration of a GRB jet may be proceeded with two mechanisms: thermally driven or magnetically driven. The former is relevant for a fireball, which proceeds rapidly; whereas the latter is relevant for a purely Poynting flux dominated outflow, and proceeds relatively more slowly. In realistic cases for both a hyper-accreting black hole or a rapidly spinning magnetar, the central engine very likely carries both components: one “hot” component due to neutrino heating from the accretion disk or the proto neutron star, and a “cold” component

related to a magnetic Poynting flux launched from the black hole or the neutron star (e.g. Lei et al. 2013; Metzger et al. 2011). The central engine can be therefore characterized by a parameter

$$\mu_0 = \frac{L_w}{\dot{M}c^2} = \frac{L_{h,0} + L_{c,0}}{\dot{M}c^2} = \eta(1 + \sigma_0), \quad (1)$$

where $L_{h,0} = \eta\dot{M}c^2$, $L_{c,0} = L_{P,0}$, and L_w are the luminosities of the hot component, cold (Poynting flux) component, and the entire wind, respectively. The dimensionless entropy η defines average total energy (rest mass energy plus thermal energy) per baryon, and the magnetization parameter σ_0 is defined as³

$$\sigma_0 \equiv \frac{L_c}{L_h} = \frac{L_P}{\eta\dot{M}c^2}. \quad (2)$$

For a variable central engine, all the parameters are a function of t . For each slice of wind materials (launched within a short time interval), all the parameters are a function of r , the radius from the central engine.

Regardless of how the parameters evolve with radius r , at any distance, one may define a parameter (Zhang 2014)

$$\mu(r) = \Gamma(r)\Theta(r)(1 + \sigma(r)), \quad (3)$$

where Γ is the bulk Lorentz factor, Θ is the total co-moving energy per baryon ($\Theta - 1$ is the thermal energy), and σ is the ratio between comoving cold (magnetic) and hot (matter) energy densities. All parameters are a function of r , and should evolve with r . If no additional baryon loading occurs and if there is no energy loss in the system, one has a conserved μ value

$$\mu = \Gamma\Theta(1 + \sigma) = \eta(1 + \sigma_0) = \mu_0 = \text{const.} \quad (4)$$

In reality, leakage of radiation energy (the GRB emission itself) is inevitable, so that one should have $\mu < \mu_0$.

The dynamical evolution (the evolution of $\Gamma(r)$ and $\sigma(r)$) of a hybrid system is not studied in detail. The jet dynamics in the two extreme cases, however, are well studied.

For $\eta \gg 1$ and $\sigma_0 \ll 1$ (a pure fireball), Γ would firstly increase linearly with r until reaching the maximum Lorentz factor defined by η (or a characteristic value η_c if $\eta > \eta_c$, Mészáros & Rees 2000), then “coasts” at the maximum value until the IS radius, where fast shells catch up slow shells and dissipate kinetic energy through shocks. After the IS phase,

³The traditional definition of σ is the ratio between the Poynting flux and the kinetic flux of matter. For the hybrid system studied in this paper, it is more convenient to also include internal energy in the matter flux in the definition of a more generalized σ .

the average Lorentz factor of the flow decreases, since a significant amount of energy is lost in the form of radiation. The ejecta keeps coasting (probably with minor decrease of Lorentz factor due to residue ISs, e.g. Li & Waxman 2008) until reaching the deceleration radius beyond which the inertia from the circumburst medium is large enough and the Lorentz factor of the blastwave decreases as a power law with radius (e.g. $\Gamma \propto r^{-3/2}$ for a constant density medium).

For $\eta \sim 1$ and $\sigma_0 \gg 1$ (a Poynting flux dominated outflow), the jet dynamics is more complicated. Generally, the flow can be quickly accelerated to a “rapid acceleration” point, which we denote r_{ra} in the rest of the paper, at which the bulk Lorentz factor exceeds the “Alfvenic” Lorentz factor,

$$\Gamma_A = (1 + \sigma)^{1/2}, \quad (5)$$

of the outflow, so that (Li et al. 1992; Komissarov et al. 2009)⁴

$$\Gamma_{\text{ra}} = (1 + \sigma_0)^{1/3} \simeq \sigma_0^{1/3} \quad (6)$$

and

$$(1 + \sigma_{\text{ra}}) = (1 + \sigma_0)^{2/3}, \quad (7)$$

or $\sigma_{\text{ra}} \simeq \sigma_0^{2/3}$. Here $\Gamma_{\text{ra}} = \Gamma(r_{\text{ra}})$ and $\sigma_{\text{ra}} = \sigma(r_{\text{ra}})$ are the Lorentz factor and σ value at r_{ra} , respectively. The acceleration law during this rapid acceleration phase is a power law, $\Gamma \propto r^\lambda$, and the power-law index λ depends on the magnetic configuration of the GRB jet, which could be from $1/2$ to 1 (e.g. Komissarov et al. 2009; Granot et al. 2011). Since the exact value does not affect the main conclusion of this work, for simplicity, we adopt $\lambda = 1$ in the rest of the discussion, so that this acceleration phase can be treated as similar to the thermally-driven case. Above r_{ra} , since σ is still $\gg 1$, continued acceleration of the ejecta is still possible. However, the acceleration is slow and delicate, depending on the detailed magnetic configuration, and whether there is significant magnetic dissipation along the way. The most rapid acceleration would have a power law form $\Gamma \propto r^{1/3}$, either due to continuous magnetic dissipation (Drenkhahn & Spruit 2002) or via an impulsive acceleration mechanism (Granot et al. 2011). In general, such a process may be described by a general acceleration law $\Gamma \propto r^\delta$ with $0 < \delta \leq 1/3$ (e.g. Mészáros & Rees 2011; Veres & Mészáros 2012). Ideally, the acceleration would continue until reaching the coasting radius r_c where Γ reaches σ_0 . However, if σ_0 is large enough, the jet may start to decelerate before the maximum Γ is reached ($r_{\text{dec}} < r_c$, e.g. Granot 2012). Furthermore, due to the internal irregularity of the outflow, multiple internal collisions within the moderately high- σ jet would trigger ICMART

⁴If the outflow is collimated to an opening angle θ_j by, say, a stellar envelope within the collapsar scenario, Γ_{ra} may increase by a factor $\theta_j^{-2/3}$, and σ_{ra} decreases by the same factor (Tchekhovskoy et al. 2009).

events to dissipate magnetic energy (Zhang & Yan 2011). This would lead to a sudden drop of σ and an abrupt increase of Γ in the emission region (e.g. Zhang & Zhang 2014). If the ejecta are individual magnetic blobs (e.g. Yuan & Zhang 2012), magnetic dissipation is facilitated since one collision would trigger significant reconnection activities (W. Deng et al. 2014, in preparation).

Since both thermal acceleration and magnetic rapid acceleration proceed approximately linearly, for a hybrid system, we approximately assume that the ejecta first gets accelerated with $\Gamma \propto r$ until reaching a more generally defined *rapid acceleration* radius r_{ra} . If $\eta > (1 + \sigma_0)^{1/2}$, after the linear acceleration phase of a fireball, the magnetized outflow's Lorentz factor already exceeds its Alfven Lorentz factor, and no rapid acceleration can be proceeded magnetically. One therefore has for $\eta > (1 + \sigma_0)^{1/2}$,

$$\begin{aligned}\Gamma_{\text{ra}} &= \frac{\eta}{\Theta_{\text{ra}}}, \\ 1 + \sigma_{\text{ra}} &= 1 + \sigma_0.\end{aligned}\tag{8}$$

Notice that σ essentially does not decrease during this phase, but the matter portion of the luminosity changes from the thermal form to the kinetic form. In the opposite regime ($\eta < (1 + \sigma_0)^{1/2}$), after the thermal acceleration phase, the outflow still moves with a Lorentz factor smaller than Γ_A (eq.(2)), so that it can still undergo rapid acceleration until $\Gamma_{\text{ra}} = \Gamma_A$ is satisfied. One therefore has for $\eta < (1 + \sigma_0)^{1/2}$

$$\begin{aligned}\Gamma_{\text{ra}} &= \left[\frac{\eta}{\Theta_{\text{ra}}} (1 + \sigma_0) \right]^{1/3}, \\ 1 + \sigma_{\text{ra}} &= \left[\frac{\eta}{\Theta_{\text{ra}}} (1 + \sigma_0) \right]^{2/3}.\end{aligned}\tag{9}$$

Putting these together, one can generally define

$$\Gamma_{\text{ra}} = \max \left(\frac{\eta}{\Theta_{\text{ra}}}, \left[\frac{\eta}{\Theta_{\text{ra}}} (1 + \sigma_0) \right]^{1/3} \right),\tag{10}$$

and

$$1 + \sigma_{\text{ra}} = \min \left(1 + \sigma_0, \left[\frac{\eta}{\Theta_{\text{ra}}} (1 + \sigma_0) \right]^{2/3} \right).\tag{11}$$

Here $\Theta_{\text{ra}} \sim 1$ is the total co-moving energy per baryon at r_{ra} .

Beyond r_{ra} , the jet would undergo a relatively slow acceleration with $\Gamma \propto r^\delta$ until reaching a *coasting radius* r_c . If one ignores radiation energy loss, the coasting Lorentz factor would be

$$\Gamma_c = \frac{\eta(1 + \sigma_0)}{\Theta_c(1 + \sigma_c)} \simeq \eta(1 + \sigma_0),\tag{12}$$

since $\Theta_c \sim 1$, and $\sigma_c \ll 1$. Here Γ_c , σ_c , and Θ_c are the Lorentz factor, magnetization parameter, and comoving energy per baryon at r_c , respectively.

In summary, if one ignores deceleration and energy loss, the Γ evolution for a hybrid system may be approximated as

$$\Gamma(r) = \begin{cases} \frac{r}{r_0}, & r_0 < r < r_{\text{ra}}; \\ \Gamma_{\text{ra}} \left(\frac{r}{r_{\text{ra}}} \right)^\delta, & r_{\text{ra}} < r < r_c; \\ \Gamma_c, & r > r_c, \end{cases} \quad (13)$$

where r_0 is the radius of the jet base (size of central engine), $r_{\text{ra}} = \Gamma_{\text{ra}} r_0$, Γ_{ra} follows eq.(10),

$$r_c = r_{\text{ra}} \left(\frac{\Gamma_c}{\Gamma_{\text{ra}}} \right)^{1/\delta}, \quad (14)$$

and Γ_c follows eq.(12).

In reality, one has to consider jet deceleration at a radius r_{dec} , as well as possible internal energy dissipation and radiation loss at the IS radius, r_{IS} (if dissipation occurs during the coasting phase), or at the ICMART radius, r_{ICMART} (if dissipation happens during the slow acceleration phase where σ is still > 1). Which situation occurs depends on the initial condition (η, σ_0) . In Figure 1, we present the evolution of Γ and σ with respect to the radius r for different input parameters. We assume the ICMART radius (r_{ICMART}) and IS radius (r_{IS}) are both at 10^{15} cm, with radius defined as r_{IS} if it is in the coasting phase, but as r_{ICMART} if it is in the slow acceleration phase. If $\sigma(r_{15}) \gg 1$, ICMART events would occur, and increase Γ and reduce σ dramatically (Zhang & Yan 2011). The deceleration radius r_{dec} here is defined where the total energy of swept-up matter from the interstellar medium (ISM) is half of the kinetic energy of the jet. We assume $E_K = 10^{52}$ erg and number density of ISM as $n = 1 \text{ cm}^{-3}$ to calculate r_{dec} . The results suggest that unless σ_0 is relatively small (say, below 80 for $\eta = 10$), the energy dissipation region (non-thermal emission region) is generally in the slow acceleration phase where $\sigma > 1$, so that ICMART rather than IS would be the main mechanism to power the observed non-thermal emission from GRBs. This point is also obvious in view that for typical parameters, the typical values of the derived r_c are all $\gg 10^{15}$ cm.

3. Photosphere emission from a hybrid jet: the bottom-up approach

The photosphere radius, r_{ph} , is defined by the condition that the photon optical depth for Thomson scattering drops below unity, so that photons previously trapped in the fireball

can escape. In the lab frame, this condition is written as

$$\tau = \int_{r_{\text{ph}}}^{\infty} n_e \sigma_{\text{T}} ds = 1, \quad (15)$$

where σ_{T} is the Thomson cross section, the lab frame electron number density can be written as

$$n_e = \frac{L_w \mathcal{V}}{4\pi r^2 m_p c^3 \eta (1 + \sigma_0)}, \quad (16)$$

and

$$ds = (1 - \beta \cos \theta) dr / \cos \theta \quad (17)$$

is the spatial increment in the outflow wind in the lab frame (e.g. eq.(23) of Deng & Zhang 2014), θ is the angle from line-of-sight, m_p is proton mass, c is speed of light, and \mathcal{V} is the lepton-to-baryon number ratio. We assume that $\mathcal{V} \ll m_p/m_e$ is satisfied, so that the inertia of the leptons is negligible. Consider the line of sight direction ($\theta = 0$), one has $ds = (1 - \beta)dr \simeq dr/(2\Gamma^2)$. For Γ evolution as shown in Equation (13), the line-of-sight photosphere radius can be derived as

$$r_{\text{ph}} = \begin{cases} \left(\frac{L_w \mathcal{V} \sigma_{\text{T}} r_0^2}{8\pi m_p c^3 \eta (1 + \sigma_0)} \right)^{1/3}, & r_0 < r_{\text{ph}} < r_{\text{ra}}; \\ \left(\frac{L_w \mathcal{V} \sigma_{\text{T}} r_{\text{ra}}^{2\delta}}{8\pi m_p c^3 \Gamma_{\text{ra}}^2 \eta (1 + \sigma_0)} \right)^{1/(2\delta+1)}, & r_{\text{ra}} < r_{\text{ph}} < r_{\text{c}}; \\ \frac{L_w \mathcal{V} \sigma_{\text{T}}}{8\pi m_p c^3 \Gamma_{\text{c}}^2 \eta (1 + \sigma_0)}, & r_{\text{ph}} > r_{\text{c}}. \end{cases} \quad (18)$$

As shown in Pe'er et al. (2007), the observed temperature and thermal flux can be derived as

$$T_{\text{ob}} = 1.48 \Gamma_{\text{ph}} T'_{\text{ph}} / (1 + z), \quad (19)$$

$$F_{\text{BB}} = \mathcal{R}^2 \sigma_{\text{SB}} T_{\text{ob}}^4, \quad (20)$$

where

$$\mathcal{R} = 1.06 \frac{(1 + z)^2 r_{\text{ph}}}{d_L \Gamma_{\text{ph}}}, \quad (21)$$

z is the redshift, d_L is the luminosity distance, σ_{SB} is the Stefan-Boltzmann constant, and T'_{ph} is the comoving temperature at the photosphere radius r_{ph} .

The evolution of T'_{ph} depends on whether significant magnetic energy dissipation happens below the photosphere radius r_{ph} . This is an open question, and no firm conclusion has been drawn from the first principles. In the following, we discuss both scenarios.

3.1. The case of no magnetic dissipation

This scenario assumes that no magnetic field reconnection occurs below the photosphere, so that no magnetic energy is directly converted to particle energy and heat. Magnetic acceleration in any case proceeds, so that some magnetic energy is converted to the kinetic energy of the outflow. Such a scenario may be relevant to helical jets or self-sustained magnetic bubbles (e.g. Spruit et al. 2001; Uzdensky & MacFadyen 2006; Yuan & Zhang 2012).

Without magnetic heating, the thermal energy undergoes adiabatic cooling, with $r^2 e^{3/4} \Gamma = \text{const}$ (e.g. Piran et al. 1993). Noticing $e \propto T'^4$ and the dynamical evolution eq.(13), one can derive the comoving temperature at the photosphere radius r_{ph} as

$$T'_{\text{ph}} = \begin{cases} T_0 \left(\frac{r_{\text{ph}}}{r_0} \right)^{-1}, & r_0 < r_{\text{ph}} < r_{\text{ra}}; \\ T_0 \left(\frac{r_{\text{ra}}}{r_0} \right)^{-1} \left(\frac{r_{\text{ph}}}{r_{\text{ra}}} \right)^{-(2+\delta)/3}, & r_{\text{ra}} < r_{\text{ph}} < r_c; \\ T_0 \left(\frac{r_{\text{ra}}}{r_0} \right)^{-1} \left(\frac{r_c}{r_{\text{ra}}} \right)^{-(2+\delta)/3} \left(\frac{r_{\text{ph}}}{r_c} \right)^{-2/3}, & r_{\text{ph}} > r_c. \end{cases} \quad (22)$$

Here

$$T_0 \simeq \left(\frac{L_w}{4\pi r_0^2 a c (1 + \sigma_0)} \right)^{1/4} \quad (23)$$

is the temperature at r_0 , $a = 7.56 \times 10^{-15} \text{ erg cm}^{-3} \text{ K}^{-4}$ is radiation density constant. Given the central engine parameters L_w , r_0 , η and σ_0 , we can derive all the relevant photosphere properties with equations from (13) to (22), as long as the slow magnetic acceleration index δ is determined. For simplification, in the rest of the paper we adopt most efficient acceleration index $\delta = 1/3$ (Drenkhahn & Spruit 2002; Granot et al. 2011; Mészáros & Rees 2011; Veres & Mészáros 2012). The theory below can be easily expanded to more general cases of the δ values. For simplicity, our analytical formulae are derived assuming $\Theta_{\text{ra}} = \Theta_c = 1$ (cold flow), and $\sigma_c = 0$.

For different central engine parameters, Γ_{ra} can have two possible values: η or $[\eta(1 + \sigma_0)]^{1/3}$. For each case, the photosphere radius r_{ph} can be in three different regimes separated by r_{ra} and r_c . So altogether we can define 6 different regimes: (I) $\eta > (1 + \sigma_0)^{1/2}$ and $r_{\text{ph}} < r_{\text{ra}}$; (II) $\eta > (1 + \sigma_0)^{1/2}$ and $r_{\text{ra}} < r_{\text{ph}} < r_c$; (III) $\eta > (1 + \sigma_0)^{1/2}$ and $r_{\text{ph}} > r_c$; (IV) $\eta < (1 + \sigma_0)^{1/2}$ and $r_{\text{ph}} < r_{\text{ra}}$; (V) $\eta < (1 + \sigma_0)^{1/2}$ and $r_{\text{ra}} < r_{\text{ph}} < r_c$; (VI) $\eta < (1 + \sigma_0)^{1/2}$ and $r_{\text{ph}} > r_c$. The 6 regimes also apply for the case with significant magnetic dissipation below the photosphere (see below). In Table 1, we list the criteria of all 12 regimes (for the cases of both without and with magnetic dissipations) based on the central engine properties. In the following, we derive relevant parameters in each regime, including r_{ra} and r_c (which are useful to write down the Γ evolution of the system), along with the photosphere properties,

i.e. r_{ph} , Γ_{ph} , $(1 + \sigma_{\text{ph}})$, T_{ob} , and F_{BB} (the presented result of T_{ob} is actually for kT_{ob} in unit of keV):

Regime I:

$$\begin{aligned}
 r_{\text{ra}} &= 1.0 \times 10^{11} \text{ cm } r_{0,9} \eta_2, \\
 r_{\text{c}} &= 1.0 \times 10^{17} \text{ cm } r_{0,9} \eta_2 (1 + \sigma_0)_2^3, \\
 r_{\text{ph}} &= 8.34 \times 10^{10} \text{ cm } L_{w,52}^{1/3} r_{0,9}^{2/3} \eta_2^{-1/3} (1 + \sigma_0)_2^{-1/3}, \\
 \Gamma_{\text{ph}} &= 83.4 L_{w,52}^{1/3} r_{0,9}^{-1/3} \eta_2^{-1/3} (1 + \sigma_0)_2^{-1/3}, \\
 1 + \sigma_{\text{ph}} &= 100(1 + \sigma_0)_2, \\
 T_{\text{ob}} &= 56.1 \text{ keV } (1 + z)^{-1} L_{w,52}^{1/4} r_{0,9}^{-1/2} (1 + \sigma_0)_2^{-1/4}, \\
 F_{\text{BB}} &= 1.07 \times 10^{-7} \text{ erg s}^{-1} \text{cm}^{-2} L_{w,52} (1 + \sigma_0)_2^{-1} d_{L,28}^{-2}.
 \end{aligned} \tag{24}$$

Regime II:

$$\begin{aligned}
 r_{\text{ra}} &= 1.0 \times 10^{11} \text{ cm } r_{0,9} \eta_2, \\
 r_{\text{c}} &= 1.0 \times 10^{17} \text{ cm } r_{0,9} \eta_2 (1 + \sigma_0)_2^3, \\
 r_{\text{ph}} &= 7.22 \times 10^{10} \text{ cm } L_{w,52}^{3/5} r_{0,9}^{2/5} \eta_2^{-7/5} (1 + \sigma_0)_2^{-3/5}, \\
 \Gamma_{\text{ph}} &= 89.7 L_{w,52}^{1/5} r_{0,9}^{-1/5} \eta_2^{1/5} (1 + \sigma_0)_2^{-1/5}, \\
 1 + \sigma_{\text{ph}} &= 17.7 L_{w,52}^{-1/5} r_{0,9}^{1/5} \eta_2^{4/5} (1 + \sigma_0)_2^{6/5}, \\
 T_{\text{ob}} &= 64.8 \text{ keV } (1 + z)^{-1} L_{w,52}^{-1/60} r_{0,9}^{-7/30} \eta_2^{16/15} (1 + \sigma_0)_2^{1/60}, \\
 F_{\text{BB}} &= 1.24 \times 10^{-7} \text{ erg s}^{-1} \text{cm}^{-2} L_{w,52}^{11/15} r_{0,9}^{4/15} \eta_2^{16/15} (1 + \sigma_0)_2^{-11/15} d_{L,28}^{-2}.
 \end{aligned} \tag{25}$$

Regime III:

$$\begin{aligned}
 r_{\text{ra}} &= 1.0 \times 10^{11} \text{ cm } r_{0,9} \eta_2, \\
 r_{\text{c}} &= 1.0 \times 10^{17} \text{ cm } r_{0,9} \eta_2 (1 + \sigma_0)_2^3, \\
 r_{\text{ph}} &= 5.81 \times 10^{12} \text{ cm } L_{w,52} \eta_1^{-3} (1 + \sigma_0)_1^{-3}, \\
 \Gamma_{\text{ph}} &= 100 \eta_1 (1 + \sigma_0)_1,
 \end{aligned}$$

$$\begin{aligned}
1 + \sigma_{\text{ph}} &\simeq 1, \\
T_{\text{ob}} &= 6.65 \text{ keV } (1+z)^{-1} L_{w,52}^{-5/12} r_{0,9}^{1/6} \eta_1^{8/3} (1+\sigma_0)_1^{29/12}, \\
F_{\text{BB}} &= 7.15 \times 10^{-8} \text{ erg s}^{-1} \text{cm}^{-2} L_{w,52}^{1/3} r_{0,9}^{2/3} \eta_1^{8/3} (1+\sigma_0)_1^{5/3} d_{L,28}^{-2}.
\end{aligned} \tag{26}$$

Regime IV:

$$\begin{aligned}
r_{\text{ra}} &= 2.15 \times 10^{10} \text{ cm } r_{0,9} \eta_2^{1/3} (1+\sigma_0)_2^{1/3}, \\
r_{\text{c}} &= 2.15 \times 10^{18} \text{ cm } r_{0,9} \eta_2^{7/3} (1+\sigma_0)_2^{7/3}, \\
r_{\text{ph}} &= 8.34 \times 10^{10} \text{ cm } L_{w,52}^{1/3} r_{0,9}^{2/3} \eta_2^{-1/3} (1+\sigma_0)_2^{-1/3}, \\
\Gamma_{\text{ph}} &= 83.4 L_{w,52}^{1/3} r_{0,9}^{-1/3} \eta_2^{-1/3} (1+\sigma_0)_2^{-1/3}, \\
1 + \sigma_{\text{ph}} &= 5.56 L_{w,52}^{-1/3} r_{0,9}^{1/3} \eta_2^{4/3} (1+\sigma_0)_2^{4/3}, \\
T_{\text{ob}} &= 56.1 \text{ keV } (1+z)^{-1} L_{w,52}^{1/4} r_{0,9}^{-1/2} (1+\sigma_0)_2^{-1/4}, \\
F_{\text{BB}} &= 1.07 \times 10^{-7} \text{ erg s}^{-1} \text{cm}^{-2} L_{w,52} (1+\sigma_0)_2^{-1} d_{L,28}^{-2}.
\end{aligned} \tag{27}$$

Regime V:

$$\begin{aligned}
r_{\text{ra}} &= 2.15 \times 10^{10} \text{ cm } r_{0,9} \eta_2^{1/3} (1+\sigma_0)_2^{1/3}, \\
r_{\text{c}} &= 2.15 \times 10^{18} \text{ cm } r_{0,9} \eta_2^{7/3} (1+\sigma_0)_2^{7/3}, \\
r_{\text{ph}} &= 2.46 \times 10^{11} \text{ cm } L_{w,52}^{3/5} r_{0,9}^{2/5} \eta_2^{-13/15} (1+\sigma_0)_2^{-13/15}, \\
\Gamma_{\text{ph}} &= 48.5 L_{w,52}^{1/5} r_{0,9}^{-1/5} \eta_2^{-1/15} (1+\sigma_0)_2^{-1/15}, \\
1 + \sigma_{\text{ph}} &= 17.7 L_{w,52}^{-1/5} r_{0,9}^{1/5} \eta_2^{16/15} (1+\sigma_0)_2^{16/15}, \\
T_{\text{ob}} &= 19.0 \text{ keV } (1+z)^{-1} L_{w,52}^{-1/60} r_{0,9}^{-7/30} \eta_2^{8/15} (1+\sigma_0)_2^{17/60}, \\
F_{\text{BB}} &= 3.63 \times 10^{-8} \text{ erg s}^{-1} \text{cm}^{-2} L_{w,52}^{11/15} r_{0,9}^{4/15} \eta_2^{8/15} (1+\sigma_0)_2^{-7/15} d_{L,28}^{-2}.
\end{aligned} \tag{28}$$

Regime VI:

$$r_{\text{ra}} = 2.15 \times 10^{10} \text{ cm } r_{0,9} \eta_2^{1/3} (1+\sigma_0)_2^{1/3},$$

$$\begin{aligned}
r_c &= 2.15 \times 10^{18} \text{ cm } r_{0,9} \eta_2^{7/3} (1 + \sigma_0)_2^{7/3}, \\
r_{\text{ph}} &= 5.81 \times 10^{12} \text{ cm } L_{w,52} \eta_1^{-3} (1 + \sigma_0)_1^{-3}, \\
\Gamma_{\text{ph}} &= 100 \eta_1 (1 + \sigma_0)_1, \\
1 + \sigma_{\text{ph}} &\simeq 1, \\
T_{\text{ob}} &= 6.65 \text{ keV } (1 + z)^{-1} L_{w,52}^{-5/12} r_{0,9}^{1/6} \eta_1^{8/3} (1 + \sigma_0)_1^{29/12}, \\
F_{\text{BB}} &= 7.15 \times 10^{-8} \text{ erg s}^{-1} \text{ cm}^{-2} L_{w,52}^{1/3} r_{0,9}^{2/3} \eta_1^{8/3} (1 + \sigma_0)_1^{5/3} d_{L,28}^{-2}.
\end{aligned} \tag{30}$$

To better present our results, we show the contour plots of T_{ob} and F_{BB} in the $(\eta, 1 + \sigma_0)$ plane in Figure 2.

3.2. The case of magnetic dissipation

It has been speculated that significant magnetic dissipation may occur during the propagation of the jet below the photosphere. Such a magnetically dissipative photosphere (e.g. Thompson 1994; Rees & Mészáros 2005; Giannios 2008; Mészáros & Rees 2011; Veres & Mészáros 2012) would lead to enhancement of photosphere emission, making the photosphere potentially as the dominant emission component in the GRB spectrum. In this section, we quantify the influence of this effect on photosphere emission.

With magnetic dissipation, the adiabatic relation no longer applies. One needs to introduce another conservation relation. One natural assumption is that the magnetic energy is converted into both thermal energy and the kinetic energy of bulk motion with fixed proportions (e.g. 1 : 1, but the exact proportions do not matter to define the temperature evolution of the system). With this assumption, in the lab frame and after the initial thermal acceleration phase, the internal energy should be proportional to Γ , so that in the comoving frame energy per baryon, $\Theta(r)$, should remain constant. This is translated to $r^2 e \Gamma = \text{const}$ (noticing that the co-moving size increases with Γ). In this case, the evolution of comoving temperature should be revised as

$$T'_{\text{ph}} = \begin{cases} T_0 \left(\frac{r_{\text{ph}}}{r_0} \right)^{-1}, & r_0 < r_{\text{ph}} < r_{\text{ra}}; \\ T_0 \left(\frac{r_{\text{ra}}}{r_0} \right)^{-1} \left(\frac{r_{\text{ph}}}{r_{\text{ra}}} \right)^{-(2+\delta)/4}, & r_{\text{ra}} < r_{\text{ph}} < r_c; \\ T_0 \left(\frac{r_{\text{ra}}}{r_0} \right)^{-1} \left(\frac{r_c}{r_{\text{ra}}} \right)^{-(2+\delta)/4} \left(\frac{r_{\text{ph}}}{r_c} \right)^{-2/3}, & r_{\text{ph}} > r_c. \end{cases} \tag{31}$$

Two remarks need to be made here. First, at $r_{\text{ph}} < r_{\text{ra}}$ (the first segment), there should be a segment in which $T' \propto r^{-3/4}$ is satisfied. This is relevant for $\eta < (1 + \sigma_0)^{1/2}$ but at $r > r_0 \eta$

(i.e. thermal acceleration is over and the flow is under rapid magnetic acceleration). The deviation from the approximate $T' \propto r^{-1}$ would be significant if $\eta \ll (1 + \sigma)^{1/2}$. However, in reality, a central engine always has a reasonably “hot” component so that $\eta \gg 1$. Also the introduction of this additional regime would not change the results substantially. We therefore do not get into the complications of introducing these trivial regimes. Second, at $r > r_c$, one has $\sigma < 1$. Heating due to magnetic dissipation becomes insignificant. One goes back to the scaling for an adiabatic outflow.

Using eq.(31), we can similarly derive the relevant parameters for the 6 regimes in the magnetic dissipation case:

Regime I:

$$\begin{aligned}
 r_{\text{ra}} &= 1.0 \times 10^{11} \text{ cm } r_{0,9} \eta_2, \\
 r_c &= 1.0 \times 10^{17} \text{ cm } r_{0,9} \eta_2 (1 + \sigma_0)_2^3, \\
 r_{\text{ph}} &= 8.34 \times 10^{10} \text{ cm } L_{w,52}^{1/3} r_{0,9}^{2/3} \eta_2^{-1/3} (1 + \sigma_0)_2^{-1/3}, \\
 \Gamma_{\text{ph}} &= 83.4 L_{w,52}^{1/3} r_{0,9}^{-1/3} \eta_2^{-1/3} (1 + \sigma_0)_2^{-1/3}, \\
 1 + \sigma_{\text{ph}} &= 100(1 + \sigma_0)_2, \\
 T_{\text{ob}} &= 56.1 \text{ kev } (1 + z)^{-1} L_{w,52}^{1/4} r_{0,9}^{-1/2} (1 + \sigma_0)_2^{-1/4}, \\
 F_{\text{BB}} &= 1.07 \times 10^{-7} \text{ erg s}^{-1} \text{cm}^{-2} L_{w,52} (1 + \sigma_0)_2^{-1} d_{L,28}^{-2}.
 \end{aligned} \tag{32}$$

Regime II:

$$\begin{aligned}
 r_{\text{ra}} &= 1.0 \times 10^{11} \text{ cm } r_{0,9} \eta_2, \\
 r_c &= 1.0 \times 10^{17} \text{ cm } r_{0,9} \eta_2 (1 + \sigma_0)_2^3, \\
 r_{\text{ph}} &= 7.22 \times 10^{10} \text{ cm } L_{w,52}^{3/5} r_{0,9}^{2/5} \eta_2^{-7/5} (1 + \sigma_0)_2^{-3/5}, \\
 \Gamma_{\text{ph}} &= 89.7 L_{w,52}^{1/5} r_{0,9}^{-1/5} \eta_2^{1/5} (1 + \sigma_0)_2^{-1/5}, \\
 1 + \sigma_{\text{ph}} &= 17.7 L_{w,52}^{-1/5} r_{0,9}^{1/5} \eta_2^{4/5} (1 + \sigma_0)_2^{6/5}, \\
 T_{\text{ob}} &= 60.8 \text{ kev } (1 + z)^{-1} L_{w,52}^{1/10} r_{0,9}^{-7/20} \eta_2^{3/5} (1 + \sigma_0)_2^{-1/10}, \\
 F_{\text{BB}} &= 9.62 \times 10^{-8} \text{ erg s}^{-1} \text{cm}^{-2} L_{w,52}^{6/5} r_{0,9}^{-1/5} \eta_2^{-4/5} (1 + \sigma_0)_2^{-6/5} d_{L,28}^{-2}.
 \end{aligned} \tag{33}$$

Regime III:

$$\begin{aligned}
r_{\text{ra}} &= 1.0 \times 10^{11} \text{ cm } r_{0,9} \eta_2, \\
r_{\text{c}} &= 1.0 \times 10^{17} \text{ cm } r_{0,9} \eta_2 (1 + \sigma_0)_2^3, \\
r_{\text{ph}} &= 5.81 \times 10^{12} \text{ cm } L_{w,52} \eta_1^{-3} (1 + \sigma_0)_1^{-3}, \\
\Gamma_{\text{ph}} &= 100 \eta_1 (1 + \sigma_0)_1, \\
1 + \sigma_{\text{ph}} &\simeq 1, \\
T_{\text{ob}} &= 25.5 \text{ keV } (1 + z)^{-1} L_{w,52}^{-5/12} r_{0,9}^{1/6} \eta_1^{8/3} (1 + \sigma_0)_1^3, \\
F_{\text{BB}} &= 1.54 \times 10^{-5} \text{ erg s}^{-1} \text{cm}^{-2} L_{w,52}^{1/3} r_{0,9}^{2/3} \eta_1^{8/3} (1 + \sigma_0)_1^4 d_{L,28}^{-2}.
\end{aligned} \tag{34}$$

Regime IV:

$$\begin{aligned}
r_{\text{ra}} &= 2.15 \times 10^{10} \text{ cm } r_{0,9} \eta_2^{1/3} (1 + \sigma_0)_2^{1/3}, \\
r_{\text{c}} &= 2.15 \times 10^{18} \text{ cm } r_{0,9} \eta_2^{7/3} (1 + \sigma_0)_2^{7/3}, \\
r_{\text{ph}} &= 8.34 \times 10^{10} \text{ cm } L_{w,52}^{1/3} r_{0,9}^{2/3} \eta_2^{-1/3} (1 + \sigma_0)_2^{-1/3}, \\
\Gamma_{\text{ph}} &= 83.4 L_{w,52}^{1/3} r_{0,9}^{-1/3} \eta_2^{-1/3} (1 + \sigma_0)_2^{-1/3}, \\
1 + \sigma_{\text{ph}} &= 5.56 L_{w,52}^{-1/3} r_{0,9}^{1/3} \eta_2^{4/3} (1 + \sigma_0)_2^{4/3}, \\
T_{\text{ob}} &= 56.1 \text{ keV } (1 + z)^{-1} L_{w,52}^{1/4} r_{0,9}^{-1/2} (1 + \sigma_0)_2^{-1/4}, \\
F_{\text{BB}} &= 1.07 \times 10^{-7} \text{ erg s}^{-1} \text{cm}^{-2} L_{w,52} (1 + \sigma_0)_2^{-1} d_{L,28}^{-2}.
\end{aligned} \tag{35}$$

Regime V:

$$\begin{aligned}
r_{\text{ra}} &= 2.15 \times 10^{10} \text{ cm } r_{0,9} \eta_2^{1/3} (1 + \sigma_0)_2^{1/3}, \\
r_{\text{c}} &= 2.15 \times 10^{18} \text{ cm } r_{0,9} \eta_2^{7/3} (1 + \sigma_0)_2^{7/3}, \\
r_{\text{ph}} &= 2.46 \times 10^{11} \text{ cm } L_{w,52}^{3/5} r_{0,9}^{2/5} \eta_2^{-13/15} (1 + \sigma_0)_2^{-13/15}, \\
\Gamma_{\text{ph}} &= 48.5 L_{w,52}^{1/5} r_{0,9}^{-1/5} \eta_2^{-1/15} (1 + \sigma_0)_2^{-1/15}, \\
1 + \sigma_{\text{ph}} &= 17.7 L_{w,52}^{-1/5} r_{0,9}^{1/5} \eta_2^{16/15} (1 + \sigma_0)_2^{16/15}, \\
T_{\text{ob}} &= 30.5 \text{ keV } (1 + z)^{-1} L_{w,52}^{1/10} r_{0,9}^{-7/20} \eta_2^{3/10} (1 + \sigma_0)_2^{1/20}, \\
F_{\text{BB}} &= 2.42 \times 10^{-7} \text{ erg s}^{-1} \text{cm}^{-2} L_{w,52}^{6/5} r_{0,9}^{-1/5} \eta_2^{-2/5} (1 + \sigma_0)_2^{-7/5} d_{L,28}^{-2}.
\end{aligned} \tag{36}$$

Regime VI:

$$\begin{aligned}
r_{\text{ra}} &= 2.15 \times 10^{10} \text{ cm } r_{0,9} \eta_2^{1/3} (1 + \sigma_0)_2^{1/3}, \\
r_{\text{c}} &= 2.15 \times 10^{18} \text{ cm } r_{0,9} \eta_2^{7/3} (1 + \sigma_0)_2^{7/3}, \\
r_{\text{ph}} &= 5.81 \times 10^{12} \text{ cm } L_{w,52} \eta_1^{-3} (1 + \sigma_0)_1^{-3}, \\
1 + \Gamma_{\text{ph}} &= 100 \eta_1 (1 + \sigma_0)_1, \\
1 + \sigma_{\text{ph}} &\simeq 1, \\
T_{\text{ob}} &= 39.8 \text{ keV } (1 + z)^{-1} L_{w,52}^{-5/12} r_{0,9}^{1/6} \eta_1^{55/18} (1 + \sigma_0)_1^{101/36}, \\
F_{\text{BB}} &= 9.24 \times 10^{-5} \text{ erg s}^{-1} \text{ cm}^{-2} L_{w,52}^{1/3} r_{0,9}^{2/3} \eta_1^{38/9} (1 + \sigma_0)_1^{29/9} d_{L,28}^{-2}.
\end{aligned} \tag{37}$$

The criteria for different regimes are also presented in Table 1, and the contour plots of T_{ob} and F_{BB} in the $(\eta, 1 + \sigma)$ plane are shown in Figure 3.

3.3. Example spectra

With the preparation above, one can simulate some example spectra of GRB prompt emission with the superposition of a thermal (from photosphere) and a non-thermal emission component. Given a set of central engine parameters $(L_w, r_0, \eta, \sigma_0)$, the thermal component can be well quantified. A detailed simulation of the non-thermal component requires the assumptions of the detailed energy dissipation mechanism and radiation mechanism. For the purpose of this paper (which focuses on photosphere emission), we introduce the non-thermal component empirically. We take the non-thermal component as a Band function with typical observed parameters (Preece et al. 2000; Zhang et al. 2011; Nava et al. 2011): $E_{\text{peak}} = 1000 \text{ keV}$, $\alpha = -1$, and $\beta = -2.2$. The normalization of the spectrum is determined by assuming that 50% of the remaining wind luminosity is converted to non-thermal emission. Such an efficiency may be relatively too high for IS model (e.g. Kumar 1999; Panaitescu et al. 1999), but would be reasonable for ICMART events (Zhang & Yan 2011). For a large parameter space, we find $\sigma > 1$ at 10^{15} cm , so that ICMART would be a more relevant energy dissipation mechanism for non-thermal emission (e.g. Fig.1). Even though no radiation mechanism is specified, we note that fast cooling synchrotron radiation at a relatively large emission radius is able to reproduce typical Band function spectra as observed (Uhm & Zhang 2014).

Some example spectra are presented in Figure 4 for different (η, σ_0) pairs as input

parameters. It is clearly shown that a diversity of spectrum as observed by *Fermi* can be reproduced, if η and σ_0 are allowed to vary in a wide range. When $\sigma_0 \ll 1$ (panels (a-c), the fireball case), the photosphere emission is bright, and one would expect a bright thermal component sticking out from the Band component. This is consistent with the results of Zhang & Pe’er (2009) and Fan (2010). In particular, when η is large enough, the spectrum is completely dominated by thermal component, similar to the case of GRB 090902B⁵. As η reduces or σ_0 increases (panels (d-i)), the photosphere component becomes sub-dominant (such as GRBs 100724B and 110721A), or even completely suppressed (such as GRB 080916C and many other bursts), as observed in many *Fermi* GRBs. Magnetic dissipation (solid lines) can enhance the photosphere emission as compared with the case without magnetic dissipation (dashed lines), sometimes making the thermal component the dominant component in the spectrum (panel d).

4. Inferring central engine parameters from the data: the top-down approach

In practice, a more interesting problem is how to use the observed data to diagnose the properties at the central engine. Pe’er et al. (2007) worked out this problem for the pure fireball model. They pointed out that if $r_{\text{ph}} > r_c$, it is possible to derive η and r_0 based on the observed data. Due to a degeneracy, this is impossible if $r_{\text{ph}} \leq r_c$, which corresponds to a very large η value.

In this section, we solve this problem for a more generalized hybrid outflow based on our results derived from the bottom-up approach.

In general, one has three observed quantities: the observed blackbody temperature T_{ob} , the observed blackbody flux F_{BB} , and the observed total flux F_{ob} (both thermal and non-thermal included). In the pure fireball model, there are three unknowns: L_w , η , and r_0 . This is why Pe’er et al. (2007) can solve for η and r_0 from the data. In the hybrid problem, another parameter σ_0 is introduced, so that altogether there are 4 unknowns. It is impossible to solve all 4 parameters from the data. On the other hand, applying the fireball method of Pe’er et al. (2007) to GRB 110721A led to curious, unreasonable parameters for η and r_0 as a function of t (Iyyani et al. 2013), suggesting that there are more parameters at play at the central engine. Physically, it is more reasonable to assume an essentially constant r_0 throughout a burst. Indeed, Ghirlanda et al. (2013) found that this is indeed the case for

⁵The power law non-thermal emission as observed in GRB 090902B would require an additional spectral component, which may be related to inverse Compton scattering of some kind (Pe’er et al. 2012). This is not modeled in this paper.

some GRBs that are of a fireball origin. For hybrid systems, it is reasonable to assume a constant value for r_0 , and use the data to infer other three parameters (which may vary for different r_0 values).

In the following, we derive constraints on the central engine parameters η and σ_0 . We define $f_\gamma = L_\gamma/L_w$, which connects the total flux F_{ob} to the wind luminosity L_w . We also define $f_{\text{th}} = F_{\text{BB}}/F_{\text{ob}}$, which can be directly measured from the data. We then express η and σ_0 in terms of the measurables T_{ob} and f_{th} , along with f_γ and r_0 , both are taken as constants and can be estimated to a typical value (e.g. $f_\gamma = 0.5$, $r_0 = 10^8$ cm).

We also derive the radius of the photosphere r_{ph} , the Lorentz factor, Γ_{ph} , and the magnetization parameter $(1 + \sigma_{\text{ph}})$ at the photosphere. We also derive the magnetization parameter at $\sim 10^{15}$ cm, $(1 + \sigma_{15})$, based on a simple $\Gamma \propto r^{1/3}$ scaling law. The idea is to check whether IS or ICMART is responsible for the non-thermal emission. If the derived $(1 + \sigma_{15})$ is smaller than 1, it means that 10^{15} cm is already in the coasting regime, and IS should be the main mechanism for non-thermal energy dissipation (e.g. Daigne et al. 2011). In this case, the real σ_{15} should be close to zero, so that $(1 + \sigma_{15}) \simeq 1$. If the derived $(1 + \sigma_{15})$ is larger than 1, it suggests that significant non-thermal emission is generated through ICMART (Zhang & Yan 2011).

4.1. The case of no magnetic dissipation

We again consider the 6 regimes studied in section 3.1. Similar to Pe’er et al. (2007), Regimes I and IV ($r_{\text{ph}} < r_{\text{ra}}$) introduce an additional degeneracy, so that central engine parameters cannot be inferred. We therefore focus on the other 4 regimes. The criteria for the 4 regimes based on observations are summarized in Table 2.

For regime II, we have

$$\begin{aligned}
 1 + \sigma_0 &= 25.5(1+z)^{4/3} \left(\frac{T_{\text{ob}}}{50 \text{ keV}} \right)^{4/3} \left(\frac{F_{\text{BB}}}{10^{-8} \text{ erg s}^{-1} \text{ cm}^{-2}} \right)^{-1/3} r_{0,9}^{2/3} f_{\text{th},-1}^{-1} f_\gamma^{-1} d_{L,28}^{-2/3}, \\
 \eta &= 74.8(1+z)^{11/12} \left(\frac{T_{\text{ob}}}{50 \text{ keV}} \right)^{11/12} \left(\frac{F_{\text{BB}}}{10^{-8} \text{ erg s}^{-1} \text{ cm}^{-2}} \right)^{1/48} r_{0,9}^{5/24} d_{L,28}^{1/24}, \\
 r_{\text{ph}} &= 1.78 \times 10^{10} \text{ cm} (1+z)^{-25/12} \left(\frac{T_{\text{ob}}}{50 \text{ keV}} \right)^{-25/12} \left(\frac{F_{\text{BB}}}{10^{-8} \text{ erg s}^{-1} \text{ cm}^{-2}} \right)^{37/48} r_{0,9}^{-7/24} d_{L,28}^{37/24}, \\
 \Gamma_{\text{ph}} &= 46.4(1+z)^{-1/12} \left(\frac{T_{\text{ob}}}{50 \text{ keV}} \right)^{-1/12} \left(\frac{F_{\text{BB}}}{10^{-8} \text{ erg s}^{-1} \text{ cm}^{-2}} \right)^{13/48} r_{0,9}^{-7/24} d_{L,28}^{13/24}.
 \end{aligned}$$

$$\begin{aligned}
1 + \sigma_{\text{ph}} &= 41.2(1+z)^{7/3} \left(\frac{T_{\text{ob}}}{50 \text{ keV}} \right)^{7/3} \left(\frac{F_{\text{BB}}}{10^{-8} \text{ erg s}^{-1} \text{ cm}^{-2}} \right)^{-7/12} r_{0,9}^{7/6} f_{\text{th},-1}^{-1} f_{\gamma}^{-1} d_{L,28}^{-7/6}. \\
1 + \sigma_{r_{15}} &= 1.08(1+z)^{59/36} \left(\frac{T_{\text{ob}}}{50 \text{ keV}} \right)^{59/36} \left(\frac{F_{\text{BB}}}{10^{-8} \text{ erg s}^{-1} \text{ cm}^{-2}} \right)^{-47/144} r_{0,9}^{77/72} f_{\text{th},-1}^{-1} f_{\gamma}^{-1} d_{L,28}^{-47/72}.
\end{aligned} \tag{38}$$

For regime III and VI, we have

$$\begin{aligned}
1 + \sigma_0 &= 5.99(1+z)^{4/3} \left(\frac{T_{\text{ob}}}{30 \text{ keV}} \right)^{4/3} \left(\frac{F_{\text{BB}}}{10^{-7} \text{ erg s}^{-1} \text{ cm}^{-2}} \right)^{-1/3} r_{0,9}^{2/3} f_{\text{th},-1}^{-1} f_{\gamma}^{-1} d_{L,28}^{-2/3}, \\
\eta &= 20.3(1+z)^{-5/6} \left(\frac{T_{\text{ob}}}{30 \text{ keV}} \right)^{-5/6} \left(\frac{F_{\text{BB}}}{10^{-7} \text{ erg s}^{-1} \text{ cm}^{-2}} \right)^{11/24} r_{0,9}^{-2/3} f_{\text{th},-1}^{3/4} f_{\gamma}^{3/4} d_{L,28}^{11/12}, \\
r_{\text{ph}} &= 4.09 \times 10^{11} \text{ cm} (1+z)^{-3/2} \left(\frac{T_{\text{ob}}}{30 \text{ keV}} \right)^{-3/2} \left(\frac{F_{\text{BB}}}{10^{-7} \text{ erg s}^{-1} \text{ cm}^{-2}} \right)^{5/8} f_{\text{th},-1}^{-1/4} f_{\gamma}^{-1/4} d_{L,28}^{5/4}, \\
\Gamma_{\text{ph}} &= 121.3(1+z)^{1/2} \left(\frac{T_{\text{ob}}}{30 \text{ keV}} \right)^{1/2} \left(\frac{F_{\text{BB}}}{10^{-7} \text{ erg s}^{-1} \text{ cm}^{-2}} \right)^{1/8} f_{\text{th},-1}^{-1/4} f_{\gamma}^{-1/4} d_{L,28}^{1/4}.
\end{aligned} \tag{39}$$

For regime V, we have

$$\begin{aligned}
1 + \sigma_0 &= 6.43(1+z)^{4/3} \left(\frac{T_{\text{ob}}}{10 \text{ keV}} \right)^{4/3} \left(\frac{F_{\text{BB}}}{10^{-9} \text{ erg s}^{-1} \text{ cm}^{-2}} \right)^{-1/3} r_{0,9}^{2/3} f_{\text{th},-1}^{-1} f_{\gamma}^{-1} d_{L,28}^{-2/3}, \\
\eta &= 105.0(1+z)^{7/6} \left(\frac{T_{\text{ob}}}{10 \text{ keV}} \right)^{7/6} \left(\frac{F_{\text{BB}}}{10^{-9} \text{ erg s}^{-1} \text{ cm}^{-2}} \right)^{5/24} r_{0,9}^{1/12} f_{\text{th},-1}^{1/2} f_{\gamma}^{1/2} d_{L,28}^{5/12}, \\
r_{\text{ph}} &= 4.62 \times 10^{10} \text{ cm} (1+z)^{-13/6} \left(\frac{T_{\text{ob}}}{10 \text{ keV}} \right)^{-13/6} \left(\frac{F_{\text{BB}}}{10^{-9} \text{ erg s}^{-1} \text{ cm}^{-2}} \right)^{17/24} r_{0,9}^{-1/4} f_{\text{th},-1}^{-1/6} f_{\gamma}^{-1/6} d_{L,28}^{17/12}, \\
\Gamma_{\text{ph}} &= 15.3(1+z)^{-1/6} \left(\frac{T_{\text{ob}}}{10 \text{ keV}} \right)^{-1/6} \left(\frac{F_{\text{BB}}}{10^{-9} \text{ erg s}^{-1} \text{ cm}^{-2}} \right)^{5/24} r_{0,9}^{-1/4} f_{\text{th},-1}^{-1/6} f_{\gamma}^{-1/6} d_{L,28}^{5/12}. \\
1 + \sigma_{\text{ph}} &= 44.2(1+z)^{8/3} \left(\frac{T_{\text{ob}}}{10 \text{ keV}} \right)^{8/3} \left(\frac{F_{\text{BB}}}{10^{-9} \text{ erg s}^{-1} \text{ cm}^{-2}} \right)^{-1/3} r_{0,9} f_{\text{th},-1}^{-1/3} f_{\gamma}^{-1/3} d_{L,28}^{-2/3}. \\
1 + \sigma_{r_{15}} &= 1.59(1+z)^{35/18} \left(\frac{T_{\text{ob}}}{10 \text{ keV}} \right)^{35/18} \left(\frac{F_{\text{BB}}}{10^{-9} \text{ erg s}^{-1} \text{ cm}^{-2}} \right)^{-7/72} r_{0,9}^{11/12} f_{\text{th},-1}^{-7/18} f_{\gamma}^{-7/18} d_{L,28}^{-7/36}.
\end{aligned} \tag{40}$$

Notice that regime VI has the identical scalings as regime III.

4.2. The case of magnetic dissipation

Here we consider the 6 regimes discussed in section 3.2. Again no solution for regimes I and IV is found. The criteria for the remaining 4 regimes based on observations are also summarized in Table 2.

For regime II, we have

$$\begin{aligned}
 1 + \sigma_0 &= 74.2(1+z)^{-1} \left(\frac{T_{\text{ob}}}{10 \text{ keV}} \right)^{-1} \left(\frac{F_{\text{BB}}}{10^{-7} \text{ erg s}^{-1} \text{ cm}^{-2}} \right)^{1/4} r_{0,9}^{-1/2} f_{\text{th},-1}^{-1} f_{\gamma}^{-1} d_{L,28}^{1/2}, \\
 \eta &= 6.63(1+z)^{3/2} \left(\frac{T_{\text{ob}}}{10 \text{ keV}} \right)^{3/2} \left(\frac{F_{\text{BB}}}{10^{-7} \text{ erg s}^{-1} \text{ cm}^{-2}} \right)^{-1/8} r_{0,9}^{1/2} d_{L,28}^{-1/4}, \\
 r_{\text{ph}} &= 1.11 \times 10^{12} \text{ cm} (1+z)^{-3/2} \left(\frac{T_{\text{ob}}}{10 \text{ keV}} \right)^{-3/2} \left(\frac{F_{\text{BB}}}{10^{-7} \text{ erg s}^{-1} \text{ cm}^{-2}} \right)^{5/8} d_{L,28}^{5/4}, \\
 \Gamma_{\text{ph}} &= 36.6(1+z)^{1/2} \left(\frac{T_{\text{ob}}}{10 \text{ keV}} \right)^{1/2} \left(\frac{F_{\text{BB}}}{10^{-7} \text{ erg s}^{-1} \text{ cm}^{-2}} \right)^{1/8} d_{L,28}^{1/4}, \\
 1 + \sigma_{\text{ph}} &= 13.5 f_{\text{th},-1}^{-1} f_{\gamma}^{-1} \\
 1 + \sigma_{r_{15}} &= 1.39(1+z)^{-1/2} \left(\frac{T_{\text{ob}}}{10 \text{ keV}} \right)^{-1/2} \left(\frac{F_{\text{BB}}}{10^{-7} \text{ erg s}^{-1} \text{ cm}^{-2}} \right)^{5/24} f_{\text{th},-1}^{-1} f_{\gamma}^{-1} d_{L,28}^{5/12}.
 \end{aligned} \tag{41}$$

For regime III, we have

$$\begin{aligned}
 1 + \sigma_0 &= 7.83(1+z)^{-1} \left(\frac{T_{\text{ob}}}{10 \text{ keV}} \right)^{-1} \left(\frac{F_{\text{BB}}}{10^{-3} \text{ erg s}^{-1} \text{ cm}^{-2}} \right)^{1/4} r_{0,9}^{-1/2} f_{\text{th},-1}^{3/4} f_{\gamma}^{3/4} d_{L,28}^{1/2}, \\
 \eta &= 28.3(1+z)^{3/2} \left(\frac{T_{\text{ob}}}{10 \text{ keV}} \right)^{3/2} \left(\frac{F_{\text{BB}}}{10^{-3} \text{ erg s}^{-1} \text{ cm}^{-2}} \right)^{-1/8} r_{0,9}^{1/2} f_{\text{th},-1}^{-1} f_{\gamma}^{-1} d_{L,28}^{-1/4}, \\
 r_{\text{ph}} &= 6.72 \times 10^{14} \text{ cm} (1+z)^{-3/2} \left(\frac{T_{\text{ob}}}{10 \text{ keV}} \right)^{-3/2} \left(\frac{F_{\text{BB}}}{10^{-3} \text{ erg s}^{-1} \text{ cm}^{-2}} \right)^{5/8} f_{\text{th},-1}^{-1/4} f_{\gamma}^{-1/4} d_{L,28}^{5/4}, \\
 \Gamma_{\text{ph}} &= 221.4(1+z)^{1/2} \left(\frac{T_{\text{ob}}}{10 \text{ keV}} \right)^{1/2} \left(\frac{F_{\text{BB}}}{10^{-3} \text{ erg s}^{-1} \text{ cm}^{-2}} \right)^{1/8} f_{\text{th},-1}^{-1/4} f_{\gamma}^{-1/4} d_{L,28}^{1/4}.
 \end{aligned} \tag{42}$$

For regime V, we have

$$1 + \sigma_0 = 74.3(1+z)^{-1} \left(\frac{T_{\text{ob}}}{10 \text{ keV}} \right)^{-1} \left(\frac{F_{\text{BB}}}{10^{-7} \text{ erg s}^{-1} \text{ cm}^{-2}} \right)^{1/4} r_{0,9}^{-1/2} f_{\text{th},-1}^{-1} f_{\gamma}^{-1} d_{L,28}^{1/2},$$

$$\begin{aligned}
\eta &= 5.11(1+z)^{7/2} \left(\frac{T_{\text{ob}}}{10 \text{ keV}} \right)^{7/2} \left(\frac{F_{\text{BB}}}{10^{-7} \text{ erg s}^{-1} \text{ cm}^{-2}} \right)^{-3/8} r_{0,9}^{5/4} f_{\text{th},-1}^{1/2} f_{\gamma}^{1/2} d_{L,28}^{-3/4}, \\
r_{\text{ph}} &= 1.21 \times 10^{12} \text{ cm} (1+z)^{-13/6} \left(\frac{T_{\text{ob}}}{10 \text{ keV}} \right)^{-13/6} \left(\frac{F_{\text{BB}}}{10^{-7} \text{ erg s}^{-1} \text{ cm}^{-2}} \right)^{17/24} r_{0,9}^{-1/4} f_{\text{th},-1}^{-1/6} f_{\gamma}^{-1/6} d_{L,28}^{17/12}, \\
\Gamma_{\text{ph}} &= 39.9(1+z)^{-1/6} \left(\frac{T_{\text{ob}}}{10 \text{ keV}} \right)^{-1/6} \left(\frac{F_{\text{BB}}}{10^{-7} \text{ erg s}^{-1} \text{ cm}^{-2}} \right)^{5/24} r_{0,9}^{-1/4} f_{\text{th},-1}^{-1/6} f_{\gamma}^{-1/6} d_{L,28}^{5/12}, \\
1 + \sigma_{\text{ph}} &= 9.52(1+z)^{8/3} \left(\frac{T_{\text{ob}}}{10 \text{ keV}} \right)^{8/3} \left(\frac{F_{\text{BB}}}{10^{-7} \text{ erg s}^{-1} \text{ cm}^{-2}} \right)^{-1/3} r_{0,9} f_{\text{th},-1}^{-1/3} f_{\gamma}^{-1/3} d_{L,28}^{-2/3}, \\
1 + \sigma_{r_{15}} &= 1.01(1+z)^{35/18} \left(\frac{T_{\text{ob}}}{10 \text{ keV}} \right)^{35/18} \left(\frac{F_{\text{BB}}}{10^{-7} \text{ erg s}^{-1} \text{ cm}^{-2}} \right)^{-7/72} r_{0,9}^{11/12} f_{\text{th},-1}^{-7/18} f_{\gamma}^{-7/18} d_{L,28}^{-7/36}.
\end{aligned} \tag{43}$$

For regime VI, we have

$$\begin{aligned}
1 + \sigma_0 &= 3.03(1+z)^{19/9} \left(\frac{T_{\text{ob}}}{1 \text{ keV}} \right)^{19/9} \left(\frac{F_{\text{BB}}}{10^{-4} \text{ erg s}^{-1} \text{ cm}^{-2}} \right)^{-5/36} r_{0,9}^{2/3} f_{\text{th},-1}^{-25/18} f_{\gamma}^{-25/18} d_{L,28}^{-5/18}, \\
\eta &= 17.3(1+z)^{-29/18} \left(\frac{T_{\text{ob}}}{1 \text{ keV}} \right)^{-29/18} \left(\frac{F_{\text{BB}}}{10^{-4} \text{ erg s}^{-1} \text{ cm}^{-2}} \right)^{19/72} r_{0,9}^{-2/3} f_{\text{th},-1}^{41/36} f_{\gamma}^{41/36} d_{L,28}^{19/36}, \\
r_{\text{ph}} &= 5.05 \times 10^{15} \text{ cm} (1+z)^{-3/2} \left(\frac{T_{\text{ob}}}{1 \text{ keV}} \right)^{-3/2} \left(\frac{F_{\text{BB}}}{10^{-4} \text{ erg s}^{-1} \text{ cm}^{-2}} \right)^{5/8} f_{\text{th},-1}^{-1/4} f_{\gamma}^{-1/4} d_{L,28}^{5/4}, \\
\Gamma_{\text{ph}} &= 52.5(1+z)^{1/2} \left(\frac{T_{\text{ob}}}{1 \text{ keV}} \right)^{1/2} \left(\frac{F_{\text{BB}}}{10^{-4} \text{ erg s}^{-1} \text{ cm}^{-2}} \right)^{1/8} f_{\text{th},-1}^{-1/4} f_{\gamma}^{-1/4} d_{L,28}^{1/4}.
\end{aligned} \tag{44}$$

5. Case study: GRB 110721A

GRB 110721A was jointly detected by the *Fermi* GBM and LAT. Axelsson et al. (2012) reported the time-dependent spectral evolution of GRB 110721A and suggested that the time-resolved emission spectra are best modeled with a combination of a Band function and a blackbody component. Based on a candidate optical counterpart (Greiner et al. 2011), Berger (2011) suggested two possible redshifts, $z = 0.382$ or $z = 3.512$, with the former preferred.

Iyyani et al. (2013) analyzed the time-resolved data of GRB 110721A and presented the time-dependent properties (including $f_{\text{th}} = F_{\text{BB}}/F_{\text{ob}}$, panel (a) of Fig.5; T_{ob} , and

$(F_{\text{BB}}/\sigma T_{\text{ob}}^4)^{1/2}$, panel (b) of Fig.5). Based on the diagnostic method of Pe’er et al. (2007), they derived $\eta(t)$ and $r_0(t)$. Some uncomfortable conclusions were obtained: First, $\eta(t)$ decreases with time, which is at odds with the IS model, which demands a time-increasing $\eta(t)$ to make strong ISs and efficient non-thermal emission. Second, r_0 was found to increase by more than 2 orders of magnitude early on and later decrease by near 1 order of magnitude. It is hard to imagine any realistic central engine that may change its size with such a large amplitude.

By applying our top-down diagnostic methods, the data can be naturally explained (Fig.5). We find that in all time bins, one has $(1 + \sigma_0) \gg 1$, so that the Pe’er et al. (2007) approach cannot be applied. The variation of the thermal emission properties in the time-resolved spectra is a result of varying (η, σ_0) pair as a function of time at the central engine. This is a more reasonable conclusion as compared with the varying r_0 result, in view that the GRB central engine is highly erratic, and it is possible that the dimensionless entropy and magnetization can vary randomly with time. Our inferred parameters depend on the assumed constant r_0 . In Fig.5 (panels c,d), we present the results of $(1 + \sigma_0)$ and η as a function of time for 3 assumed r_0 : 10^8 (plus), 10^9 (square), and 10^{10} (cross) cm. The results also depend on whether significant magnetic dissipation occurs below the photosphere. Given the same level of observed thermal emission, the case with significant magnetic dissipation (black) demands a larger initial magnetization $(1 + \sigma_0)$ than the case without (pink). We also plot the photosphere radius r_{ph} and photosphere Lorentz factor Γ_{ph} as a function of t for all the cases (panels e,f) of Fig.5. It is interesting to see that the derived $(1 + \sigma_0)$ initially increases with time, which is consistent with the expectation of some central engine models (e.g. Metzger et al. 2011, W.-H. Lei et al. 2014, in preparation). It is also interesting to note that Γ_{ph} initially rises with time, in contrast to the case of the pure fireball model (Iyyani et al. 2013). This is a more natural picture for both IS and ICMART scenarios. For this case, $(1 + \sigma_{15})$ is found to be above unity for some time bins, especially when magnetic dissipation is considered. This suggests that ICMART rather than IS is the mechanism to power the non-thermal emission for at least some, and probably all time bins (even if σ_{15} is smaller, but not much smaller than unity, IS is still inefficient, and ICMART can enhance energy dissipation). Based on the results in Section 4, we find that $(1 + \sigma_{15})$ tends to be larger for a larger r_0 . This is confirmed from the analysis of this burst.

6. Conclusions and Discussion

The central engine of GRB jets is most likely a hybrid system with both a hot “fireball” component and a cold Poynting flux component. In this work, we develop an analytical

theory to quantify the properties of the photosphere emission of such a hybrid system. Based on an approximate dynamical evolution model of the hybrid system, we develop a “bottom-up” approach to predict the temperature and luminosity of the photosphere emission for arbitrary input parameters, especially η and σ_0 . We consider the cases of both with and without significant magnetic dissipation during the acceleration of the jet. We show that a variety of observed GRB prompt emission spectra by *Fermi* can be reproduced given η and σ_0 are allowed to vary in a wide range (Fig.4). We also develop a “top-down” approach to diagnose η and σ_0 using the observational data. We apply the method to GRB 110721A and draw the conclusion that the central engine of the source as well as its photosphere is highly magnetized, and that the non-thermal emission is likely produced via magnetic dissipation (ICMART) rather than internal shocks. The rapid evolution of the photosphere emission properties is a result of rapid evolution of (η, σ_0) pairs rather than rapid evolution of r_0 (cf. Iyyani et al. 2013). We recommend to apply our method to diagnose a large sample of *Fermi* GRBs with the detection of the photosphere component, so as to carry out a statistical analysis of the central engine properties of a large sample of GRBs. This would have interesting implications in diagnosing the composition of GRB jets as well as inferring the mechanisms of GRB jet energy dissipation and radiation.

It is useful to comment on the relationship between our work and several previous papers. Pe’er et al. (2007) were the first to propose to diagnose central engine parameters using the observed photosphere emission properties. Their method is within the standard fireball framework. Our general diagnostic method is consistent with Pe’er et al. (2007) when $\sigma_0 \ll 1$ is assumed. Veres & Mészáros (2012) introduced the slow acceleration segment in a magnetically dominated flow to calculate the properties of the dissipative photosphere. Their photosphere radius is within the $\Gamma \propto R^{1/3}$ regime (i.e. our regimes II and V). However, they did not introduce the $(1 + \sigma_{\text{ph}})$ parameter to suppress the photosphere luminosity. This is valid when $\sigma_{\text{ph}} \sim 1$ (or $r_{\text{ph}} \sim r_c$), but would over-estimate the photosphere brightness in more general cases. Hascoët et al. (2013) introduced a parameter to denote the fraction of thermal energy at the central engine, and calculated the brightness of the photosphere emission, and assumed that the non-thermal emission is from the ISs. However, they did not explicitly take into account the dynamical evolution of a high- σ outflow. As shown in this paper, in order to reproduce the photosphere properties of the data (or upper limits), σ_0 is such that the coasting radius is usually above the IS radius. This suggests that ISs cannot operate efficiently, and significant jet energy dissipation has to proceed through magnetic dissipation processes such as ICMART. Based on the theoretical framework of Hascoët et al. (2013), Guiriec et al. (2013) presented a method to infer r_0 , η and r_{ph} using observed quantities (their eqs.(3-5)). Their results agree with our regimes III and VI without magnetic dissipation (the coasting regime). They applied the method to the short GRB 120323A and obtained an

anomalously low γ -ray efficiency. It is likely the photosphere radius is in the slow magnetic acceleration regime, so that their diagnostic method should be replaced by ours in the regimes II and V. This would alleviate the low efficiency problem encountered by the burst. Finally, Peng et al. (2014) recently discovered a sub-dominant thermal component in the X-ray flares of some GRBs with a typical temperature of a few keV. According to Figures 2 and 3, a low temperature, low flux thermal component typically requires a large σ_0 . This is consistent with the theoretical argument that a magnetic mechanism has to play an important role to power an X-ray flare jet (Fan et al. 2005).

Finally, we’d like to point out several caveats of our approach. First, we have introduced a simple analytical description of the rapid acceleration phase of a hybrid jet. Since fireball acceleration is very efficient, we assume that it would proceed first, and magnetic acceleration would take over when the dimensionless entropy is used up. In reality the acceleration of a hybrid system in the rapid acceleration phase would be more complicated, requiring to solve a set of MHD equations with the contribution of a radiation force (e.g. Russo & Thompson 2013). The solution may deviate from the simple linear acceleration assumption adopted here. In any case, since in most cases r_{ph} is above r_{ra} , the approaches derived here should give correct results to order of magnitude. Another issue of approach is the acceleration index δ during the slow acceleration phase. It depends on the global magnetic configuration, and can be delicate. The $1/3$ value adopted in our calculation is the most optimistic case for magnetic acceleration. More general expressions can be derived for an arbitrary δ ($0 < \delta < 1/3$). With these shallower acceleration profiles, the photosphere would be more magnetized, and it is even more difficult to reach the coasting phase before deceleration, so that the parameter space for ISs to operate is further reduced. In any case, ICMART should be the main mechanism to power bright non-thermal emission from many GRBs.

This work is partially supported by NASA through grant NNX14AF85G.

REFERENCES

- Abdo, A. A., Ackermann, M., Ajello, M., et al. 2009a, *ApJ*, 706, L138
- Abdo, A. A., Ackermann, M., Arimoto, M., et al. 2009b, *Science*, 323, 1688
- Atwood, W. B., Abdo, A. A., Ackermann, M., et al. 2009, *ApJ*, 697, 1071
- Axelsson, M., Baldini, L., Barbiellini, G., et al. 2012, *ApJ*, 757, L31
- Band, D., Matteson, J., Ford, L., et al. 1993, *ApJ*, 413, 281

- Beloborodov, A. M. 2010, MNRAS, 407, 1033
- Berger, E. 2011, GRB Coordinates Network, 12193, 1
- Daigne, F., & Mochkovitch, R. 1998, MNRAS, 296, 275
- Daigne, F., & Mochkovitch, R. 2002, MNRAS, 336, 1271
- Daigne, F., Bošnjak, Ž., & Dubus, G. 2011, A&A, 526, A110
- Deng, W., & Zhang, B. 2014, ApJ, 785, 112
- Drenkhahn, G., & Spruit, H. C. 2002, A&A, 391, 1141
- Fan, Y. Z., Zhang, B., & Proga, D. 2005, ApJ, 635, L129
- Fan, Y.-Z. 2010, MNRAS, 403, 483
- Ghirlanda, G., Celotti, A., & Ghisellini, G. 2002, A&A, 393, 409
- Ghirlanda, G., Celotti, A., & Ghisellini, G. 2003, A&A, 406, 879
- Ghirlanda, G., Pescalli, A., & Ghisellini, G. 2013, MNRAS, 432, 3237
- Giannios, D. 2008, A&A, 480, 305
- Giannios, D. 2012, MNRAS, 422, 3092
- Goodman, J. 1986, ApJ, 308, L47
- Granot, J., Komissarov, S. S., & Spitkovsky, A. 2011, MNRAS, 411, 1323
- Granot, J. 2012, MNRAS, 421, 2442
- Greiner, J., Utdike, A. C., Kruehler, T., & Sudilovsky, V. 2011, GRB Coordinates Network, 12192, 1
- Guiriec, S., Connaughton, V., Briggs, M. S., et al. 2011, ApJ, 727, L33
- Guiriec, S., Daigne, F., Hascoët, R., et al. 2013, ApJ, 770, 32
- Hascoët, R., Daigne, F., & Mochkovitch, R. 2013, A&A, 551, A124
- Ioka, K. 2010, Progress of Theoretical Physics, 124, 667
- Iyyani, S., Ryde, F., Axelsson, M., et al. 2013, MNRAS, 433, 2739

- Komissarov, S. S., Vlahakis, N., Königl, A., & Barkov, M. V. 2009, MNRAS, 394, 1182
- Kumar, P. 1999, ApJ, 523, L113
- Lazzati, D., & Begelman, M. C. 2010, ApJ, 725, 1137
- Lei, W.-H., Zhang, B., & Liang, E.-W. 2013, ApJ, 765, 125
- Li, Z.-Y., Chiueh, T., & Begelman, M. C. 1992, ApJ, 394, 459
- Li, Z., & Waxman, E. 2008, ApJ, 674, L65
- Lloyd, N. M., & Petrosian, V. 2000, ApJ, 543, 722
- Lundman, C., Pe’er, A., & Ryde, F. 2013, MNRAS, 428, 2430
- Lyutikov, M., & Blandford, R. 2003, arXiv:astro-ph/0312347
- Mészáros, P., Laguna, P., & Rees, M. J. 1993, ApJ, 415, 181
- Mészáros, P., & Rees, M. J. 1993, ApJ, 405, 278
- Mészáros, P., Rees, M. J., & Papathanassiou, H. 1994, ApJ, 432, 181
- Mészáros, P., & Rees, M. J. 1997, ApJ, 482, L29
- Mészáros, P., & Rees, M. J. 2000, ApJ, 530, 292
- Mészáros, P., Ramirez-Ruiz, E., Rees, M. J., & Zhang, B. 2002, ApJ, 578, 812
- Mészáros, P., & Rees, M. J. 2011, ApJ, 733, L40
- Meegan, C., Lichti, G., Bhat, P. N., et al. 2009, ApJ, 702, 791
- Metzger, B. D., Giannios, D., Thompson, T. A., Bucciantini, N., & Quataert, E. 2011, MNRAS, 413, 2031
- Nava, L., Ghirlanda, G., Ghisellini, G., & Celotti, A. 2011, A&A, 530, A21
- Paczynski, B. 1986, ApJ, 308, L43
- Panaitescu, A., Spada, M., & Mészáros, P. 1999, ApJ, 522, L105
- Pe’er, A., Mészáros, P., & Rees, M. J. 2006, ApJ, 642, 995
- Pe’er, A., Ryde, F., Wijers, R. A. M. J., Mészáros, P., & Rees, M. J. 2007, ApJ, 664, L1

- Pe’er, A., & Ryde, F. 2011, *ApJ*, 732, 49
- Pe’Er, A., Zhang, B.-B., Ryde, F., et al. 2012, *MNRAS*, 420, 468
- Peng, F.-K., Liang, E.-W., Wang, X.-Y., et al. 2014, *ApJ* Submitted
- Piran, T., Shemi, A., & Narayan, R. 1993, *MNRAS*, 263, 861
- Preece, R. D., Briggs, M. S., Mallozzi, R. S., et al. 2000, *ApJS*, 126, 19
- Preece, R., Burgess, J. M., von Kienlin, A., et al. 2014, *Science*, 343, 51
- Rees, M. J., & Mészáros, P. 1992, *MNRAS*, 258, 41P
- Rees, M. J., & Mészáros, P. 1994, *ApJ*, 430, L93
- Rees, M. J., & Mészáros, P. 2005, *ApJ*, 628, 847
- Russo, M., & Thompson, C. 2013, *ApJ*, 773, 99
- Ryde, F. 2005, *ApJ*, 625, L95
- Ryde, F., & Pe’er, A. 2009, *ApJ*, 702, 1211
- Ryde, F., Axelsson, M., Zhang, B. B., et al. 2010, *ApJ*, 709, L172
- Shemi, A., & Piran, T. 1990, *ApJ*, 365, L55
- Spruit, H. C., Daigne, F., & Drenkhahn, G. 2001, *A&A*, 369, 694
- Tavani, M. 1996, *ApJ*, 466, 768
- Tchekhovskoy, A., McKinney, J. C., & Narayan, R. 2009, *ApJ*, 699, 1789
- Thompson, C. 1994, *MNRAS*, 270, 480
- Uhm, Z. L., & Zhang, B. 2014, *Nature Physics*, 10, 351
- Usov, V. V. 1994, *MNRAS*, 267, 1035
- Uzdensky, D. A., & MacFadyen, A. I. 2006, *ApJ*, 647, 1192
- Veres, P., & Mészáros, P. 2012, *ApJ*, 755, 12
- Veres, P., Zhang, B.-B., & Mészáros, P. 2012, *ApJ*, 761, L18
- Vurm, I., Beloborodov, A. M., & Poutanen, J. 2011, *ApJ*, 738, 77

- Yuan, F., & Zhang, B. 2012, ApJ, 757, 56
- Zhang, B.-B., Zhang, B., Liang, E.-W., et al. 2011, ApJ, 730, 141
- Zhang, B., & Mészáros, P. 2002, ApJ, 581, 1236
- Zhang, B., & Pe’er, A. 2009, ApJ, 700, L65
- Zhang, B., & Yan, H. 2011, ApJ, 726, 90
- Zhang, B. 2011, Comptes Rendus Physique, 12, 206
- Zhang, B., Lu, R.-J., Liang, E.-W., & Wu, X.-F. 2012, ApJ, 758, L34
- Zhang, B. 2014, International Journal of Modern Physics D, 23, 30002
- Zhang, B., & Zhang, B. 2014, ApJ, 782, 92

| | $r_{\text{ph}} < r_{\text{ra}}$ | $r_{\text{ra}} < r_{\text{ph}} < r_{\text{c}}$ | $r_{\text{ph}} > r_{\text{c}}$ |
|-------------------------------|--|---|---|
| Non-dissipation | Regime I | Regime II | Regime III |
| $\eta > (1 + \sigma_0)^{1/2}$ | $\eta^{12/5}(1 + \sigma_0)^{3/5} > 7.22 \times 10^5 L_{w,52}^{3/5} r_{0,9}^{-3/5}$ | $\eta^{12/5}(1 + \sigma_0)^{3/5} < 7.22 \times 10^5 L_{w,52}^{3/5} r_{0,9}^{-3/5}$ $\eta^{12/5}(1 + \sigma_0)^{18/5} > 7.22 \times 10^5 L_{w,52}^{3/5} r_{0,9}^{-3/5}$ | $\eta^{12/5}(1 + \sigma_0)^{18/5} < 7.22 \times 10^5 L_{w,52}^{3/5} r_{0,9}^{-3/5}$ |
| Non-dissipation | Regime IV | Regime V | Regime VI |
| $\eta < (1 + \sigma_0)^{1/2}$ | $\eta^{6/5}(1 + \sigma_0)^{6/5} > 7.22 \times 10^5 L_{w,52}^{3/5} r_{0,9}^{-3/5}$ | $\eta^{6/5}(1 + \sigma_0)^{6/5} < 7.22 \times 10^5 L_{w,52}^{3/5} r_{0,9}^{-3/5}$ $\eta^{16/5}(1 + \sigma_0)^{16/5} > 7.22 \times 10^5 L_{w,52}^{3/5} r_{0,9}^{-3/5}$ | $\eta^{16/5}(1 + \sigma_0)^{16/5} < 7.22 \times 10^5 L_{w,52}^{3/5} r_{0,9}^{-3/5}$ |
| Dissipation | Regime I | Regime II | Regime III |
| $\eta > (1 + \sigma_0)^{1/2}$ | $\eta^{12/5}(1 + \sigma_0)^{3/5} > 7.22 \times 10^5 L_{w,52}^{3/5} r_{0,9}^{-3/5}$ | $\eta^{12/5}(1 + \sigma_0)^{3/5} < 7.22 \times 10^5 L_{w,52}^{3/5} r_{0,9}^{-3/5}$ $\eta^{12/5}(1 + \sigma_0)^{18/5} > 7.22 \times 10^5 L_{w,52}^{3/5} r_{0,9}^{-3/5}$ | $\eta^{12/5}(1 + \sigma_0)^{18/5} < 7.22 \times 10^5 L_{w,52}^{3/5} r_{0,9}^{-3/5}$ |
| Dissipation | Regime IV | Regime V | Regime VI |
| $\eta < (1 + \sigma_0)^{1/2}$ | $\eta^{6/5}(1 + \sigma_0)^{6/5} > 7.22 \times 10^5 L_{w,52}^{3/5} r_{0,9}^{-3/5}$ | $\eta^{6/5}(1 + \sigma_0)^{6/5} < 7.22 \times 10^5 L_{w,52}^{3/5} r_{0,9}^{-3/5}$ $\eta^{16/5}(1 + \sigma_0)^{16/5} > 7.22 \times 10^5 L_{w,52}^{3/5} r_{0,9}^{-3/5}$ | $\eta^{16/5}(1 + \sigma_0)^{16/5} < 7.22 \times 10^5 L_{w,52}^{3/5} r_{0,9}^{-3/5}$ |

 Table 1: Definition and theoretical criteria of r_{ph} regimes for different models.

| | |
|--|--|
| No dissipation Regime II | |
| $14.8(1+z)^{1/4}(\frac{T_{\text{ob}}}{50 \text{ keV}})^{1/4}(\frac{F_{\text{BB}}}{10^{-8} \text{ erg s}^{-1} \text{ cm}^{-2}})^{3/16}r_{0,9}^{-1/8}f_{\text{th},-1}^{1/2}f_{\gamma}^{1/2}d_{L,28}^{3/8} > 1$ | |
| $0.24(1+z)^{-3}(\frac{T_{\text{ob}}}{50 \text{ keV}})^{-3}(\frac{F_{\text{BB}}}{10^{-8} \text{ erg s}^{-1} \text{ cm}^{-2}})^{3/4}r_{0,9}^{-3/2}d_{L,28}^{3/2} > 1$ | |
| $1.43 \times 10^{-5}(1+z)^{-7}(\frac{T_{\text{ob}}}{50 \text{ keV}})^{-7}(\frac{F_{\text{BB}}}{10^{-8} \text{ erg s}^{-1} \text{ cm}^{-2}})^{7/4}r_{0,9}^{-7/2}f_{\text{th},-1}^3f_{\gamma}^3d_{L,28}^{7/2} < 1$ | |
| No dissipation Regime III | |
| $8.28(1+z)^{-3/2}(\frac{T_{\text{ob}}}{30 \text{ keV}})^{-3/2}(\frac{F_{\text{BB}}}{10^{-7} \text{ erg s}^{-1} \text{ cm}^{-2}})^{5/8}r_{0,9}^{-1}f_{\text{th},-1}^{5/4}f_{\gamma}^{5/4}d_{L,28}^{5/4} > 1$ | |
| $9.42 \times 10^{-2}(1+z)^{-14/3}(\frac{T_{\text{ob}}}{30 \text{ keV}})^{-14/3}(\frac{F_{\text{BB}}}{10^{-7} \text{ erg s}^{-1} \text{ cm}^{-2}})^{7/6}r_{0,9}^{-7/3}f_{\text{th},-1}^2f_{\gamma}^2d_{L,28}^{7/3} > 1$ | |
| Non-dissipation Regime V | |
| $41.4(1+z)^{1/2}(\frac{T_{\text{ob}}}{10 \text{ keV}})^{1/2}(\frac{F_{\text{BB}}}{10^{-9} \text{ erg s}^{-1} \text{ cm}^{-2}})^{3/8}r_{0,9}^{-1/4}f_{\text{th},-1}f_{\gamma}d_{L,28}^{3/4} < 1$ | |
| $5.28(1+z)^{-3}(\frac{T_{\text{ob}}}{10 \text{ keV}})^{-3}(\frac{F_{\text{BB}}}{10^{-9} \text{ erg s}^{-1} \text{ cm}^{-2}})^{3/4}r_{0,9}^{-3/2}d_{L,28}^{3/2} > 1$ | |
| $1.16 \times 10^{-5}(1+z)^{-8}(\frac{T_{\text{ob}}}{10 \text{ keV}})^{-8}(\frac{F_{\text{BB}}}{10^{-9} \text{ erg s}^{-1} \text{ cm}^{-2}})^{-3}r_{0,9}^{-3}f_{\text{th},-1}f_{\gamma}d_{L,28}^2 < 1$ | |
| Non-dissipation Regime VI | |
| $8.28(1+z)^{-3/2}(\frac{T_{\text{ob}}}{30 \text{ keV}})^{-3/2}(\frac{F_{\text{BB}}}{10^{-7} \text{ erg s}^{-1} \text{ cm}^{-2}})^{5/8}r_{0,9}^{-1}f_{\text{th},-1}^{5/4}f_{\gamma}^{5/4}d_{L,28}^{5/4} < 1$ | |
| $5.63 \times 10^{-3}(1+z)^{-8/3}(\frac{T_{\text{ob}}}{30 \text{ keV}})^{-8/3}(\frac{F_{\text{BB}}}{10^{-7} \text{ erg s}^{-1} \text{ cm}^{-2}})^{1/3}r_{0,9}^{-1}f_{\text{th},-1}^{1/3}f_{\gamma}^{1/3}d_{L,28}^{2/3} > 1$ | |
| Dissipation Regime II | |
| $0.77(1+z)^2(\frac{T_{\text{ob}}}{10 \text{ keV}})^2(\frac{F_{\text{BB}}}{10^{-7} \text{ erg s}^{-1} \text{ cm}^{-2}})^{-1/4}r_{0,9}^{3/4}f_{\text{th},-1}^{1/2}f_{\gamma}^{1/2}d_{L,28}^{-1/2} > 1$ | |
| $167.1(1+z)^{-3}(\frac{T_{\text{ob}}}{10 \text{ keV}})^{-3}(\frac{F_{\text{BB}}}{10^{-7} \text{ erg s}^{-1} \text{ cm}^{-2}})^{3/4}r_{0,9}^{-3/2}d_{L,28}^{3/2} > 1$ | |
| $4.09 \times 10^{-4}f_{\text{th},-1}^3f_{\gamma}^3 < 1$ | |
| Dissipation Regime III | |
| $10.1(1+z)^2(\frac{T_{\text{ob}}}{10 \text{ keV}})^2(\frac{F_{\text{BB}}}{10^{-3} \text{ erg s}^{-1} \text{ cm}^{-2}})^{-1/4}r_{0,9}^{3/4}f_{\text{th},-1}^{-11/8}f_{\gamma}^{-11/8}d_{L,28}^{-1/2} > 1$ | |
| $49.4f_{\text{th},-1}^{-3/2}f_{\gamma}^{-3/2} > 1$ | |
| Dissipation Regime V | |
| $0.59(1+z)^4(\frac{T_{\text{ob}}}{10 \text{ keV}})^4(\frac{F_{\text{BB}}}{10^{-7} \text{ erg s}^{-1} \text{ cm}^{-2}})^{-1/2}r_{0,9}^{3/2}f_{\text{th},-1}f_{\gamma}d_{L,28}^{-1} < 1$ | |
| $167.0(1+z)^{-3}(\frac{T_{\text{ob}}}{10 \text{ keV}})^{-3}(\frac{F_{\text{BB}}}{10^{-7} \text{ erg s}^{-1} \text{ cm}^{-2}})^{3/4}r_{0,9}^{-3/2}d_{L,28}^{3/2} > 1$ | |
| $1.16 \times 10^{-3}(1+z)^{-8}(\frac{T_{\text{ob}}}{10 \text{ keV}})^{-8}(\frac{F_{\text{BB}}}{10^{-7} \text{ erg s}^{-1} \text{ cm}^{-2}})^{-3}r_{0,9}^{-3}f_{\text{th},-1}f_{\gamma}d_{L,28}^2 < 1$ | |
| Dissipation Regime VI | |
| $9.95(1+z)^{-8/3}(\frac{T_{\text{ob}}}{1 \text{ keV}})^{-8/3}(\frac{F_{\text{BB}}}{10^{-4} \text{ erg s}^{-1} \text{ cm}^{-2}})^{1/3}r_{0,9}^{-1}f_{\text{th},-1}^{11/6}f_{\gamma}^{11/6}d_{L,28}^{2/3} < 1$ | |
| $490.2(1+z)^{-8/3}(\frac{T_{\text{ob}}}{1 \text{ keV}})^{-8/3}(\frac{F_{\text{BB}}}{10^{-4} \text{ erg s}^{-1} \text{ cm}^{-2}})^{1/3}r_{0,9}^{-1}f_{\text{th},-1}^{1/3}f_{\gamma}^{1/3}d_{L,28}^{2/3} > 1$ | |

Table 2: Observational criteria of r_{ph} regimes for different models.

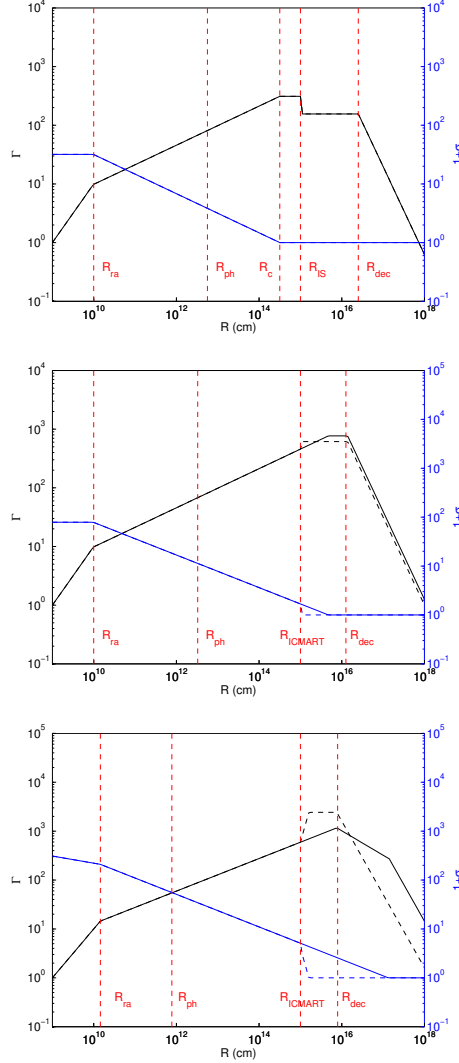


Fig. 1.— Examples of GRB jet dynamics. Black lines are for Γ evolution and blue lines are for σ evolution. Vertical dashed lines denote some characteristic radii: rapid acceleration radius r_{ra} , photosphere radius r_{ph} , coasting radius r_c , internal shock radius r_{IS} , ICMART radius r_{ICMART} , and deceleration radius r_{dec} . Following parameters are adopted: $L_w = 10^{52} \text{erg s}^{-1}$, and $r_0 = 10^9 \text{cm}$. Different panels correspond to different combinations of η and σ_0 . Top panel: $\eta = 10$ and $\sigma_0 = 30$. Internal shocks can form, which dissipate energy and reduce the total kinetic energy in the system; Middle panel: $\eta = 10$ and $\sigma_0 = 80$; Bottom panel, $\eta = 10$ and $\sigma_0 = 300$. In both cases, σ is above unity at 10^{15}cm , suggesting that ICMART events may be the main mechanism to dissipate magnetic energy and power non-thermal radiation. The dashed lines denote the consequences of ICMART events: an abrupt reduction of σ and a sudden acceleration of the system (Zhang & Yan 2011).

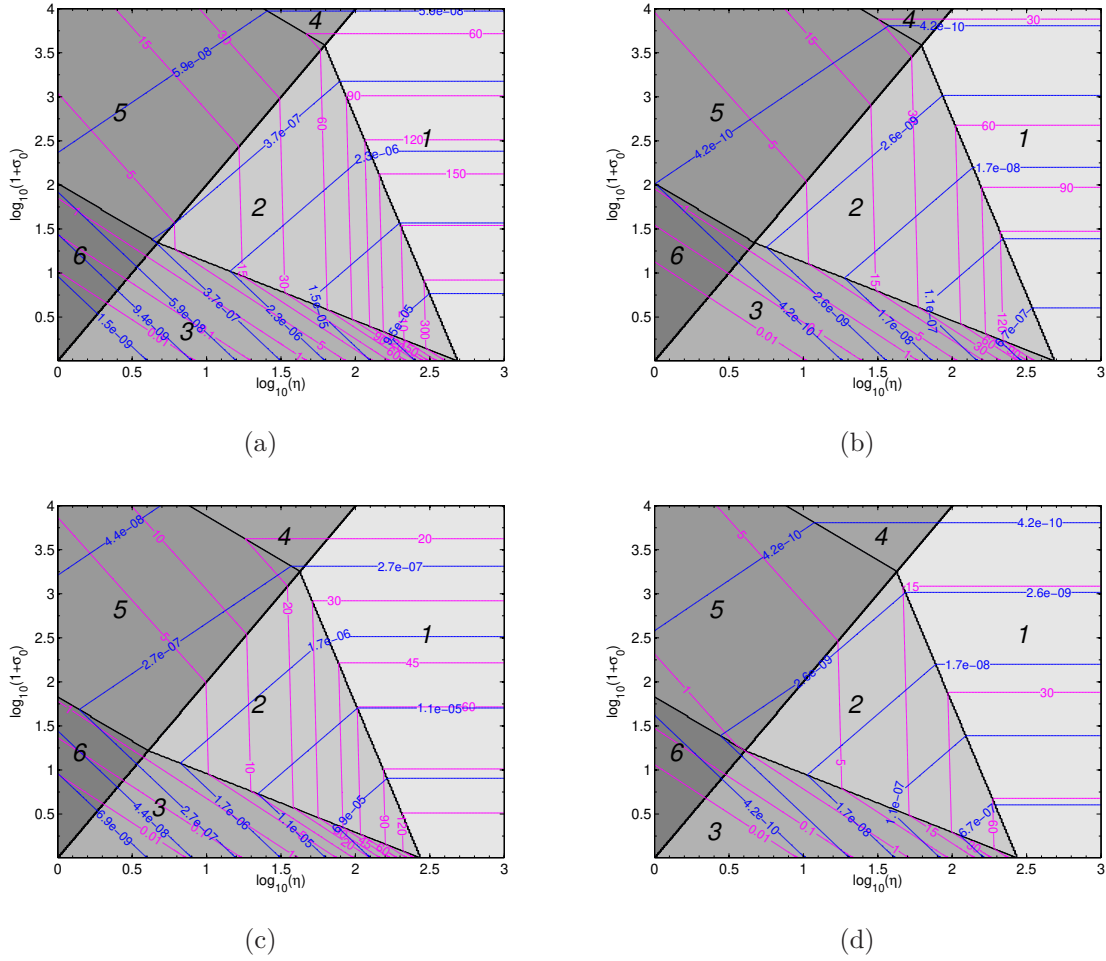


Fig. 2.— Contour plots of T_{ob} and F_{BB} in the $(\eta, 1+\sigma)$ domain. The case for the no magnetic dissipation scenario. Pink lines are for T_{ob} in units of keV, and blue lines are for F_{BB} in units of $\text{erg cm}^{-2} \text{ s}^{-1}$. The six regimes for the photosphere radius are shown in different grey blocks, with higher regime number ones marked with darker grey and the regime number marked in the block. For all the examples, $L_w = 10^{52} \text{ erg s}^{-1}$ is assumed. Top (bottom) panels are for $r_0 = 10^8 \text{ cm}$ ($r_0 = 10^9 \text{ cm}$), respectively; and left (right) panels are for $z = 0.1$ ($z = 1$), respectively.

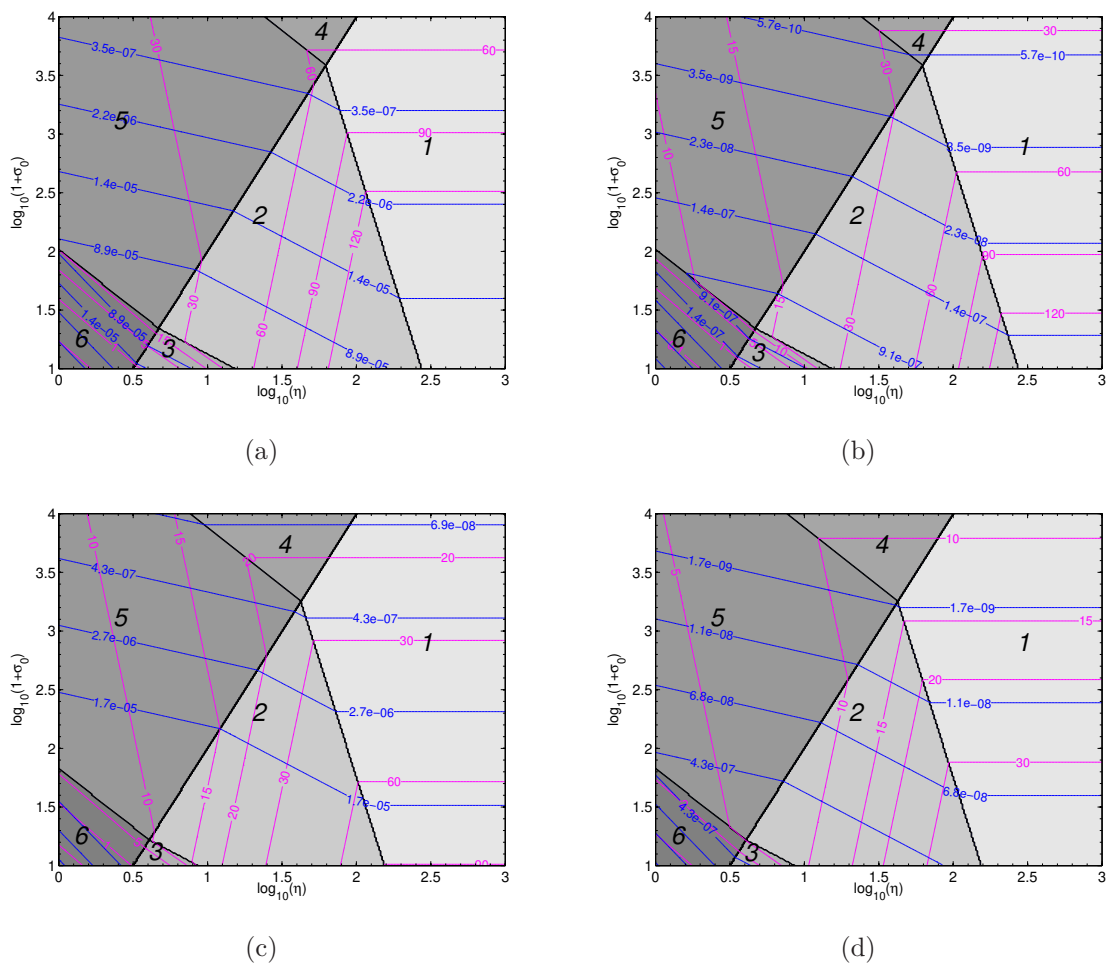


Fig. 3.— Same as Figure 2 but for the scenario with magnetic dissipation. The notation conventions are the same as Fig.2.

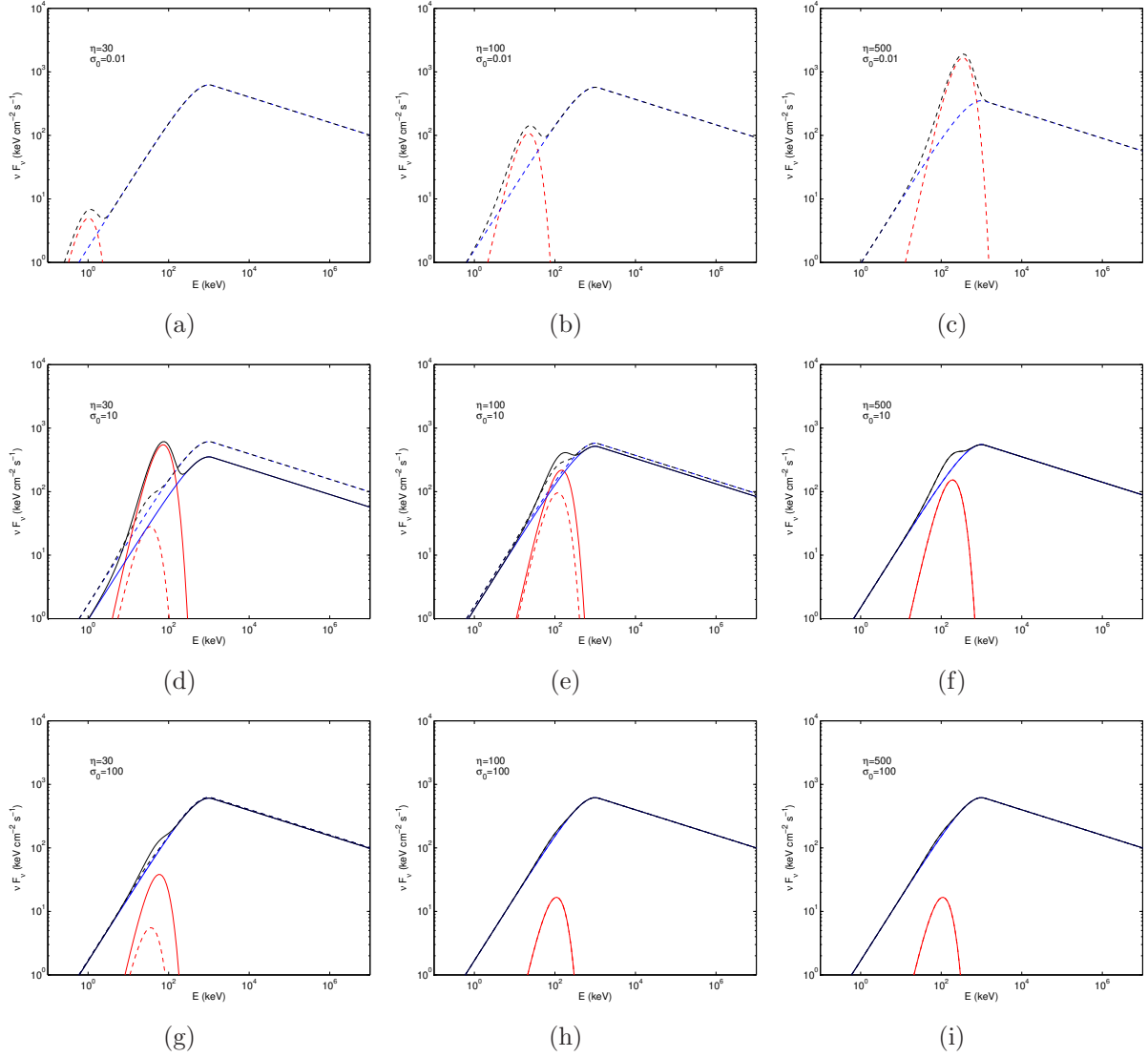


Fig. 4.— Example model spectra of GRB prompt emission. Red, blue and black lines are for thermal, non-thermal, and total spectral components, respectively. Dashed lines are for the case of no magnetic dissipation, whereas solid lines are for the case of magnetic dissipation. Here we adopt $L_w = 10^{52} \text{erg s}^{-1}$, $r_0 = 10^9 \text{cm}$, and $z = 1$. Different panels correspond to different combination of η and σ_0 (as marked in the inset of each panel). The non-thermal radiation efficiency is assumed as 50%, and a typical Band function shape is adopted.

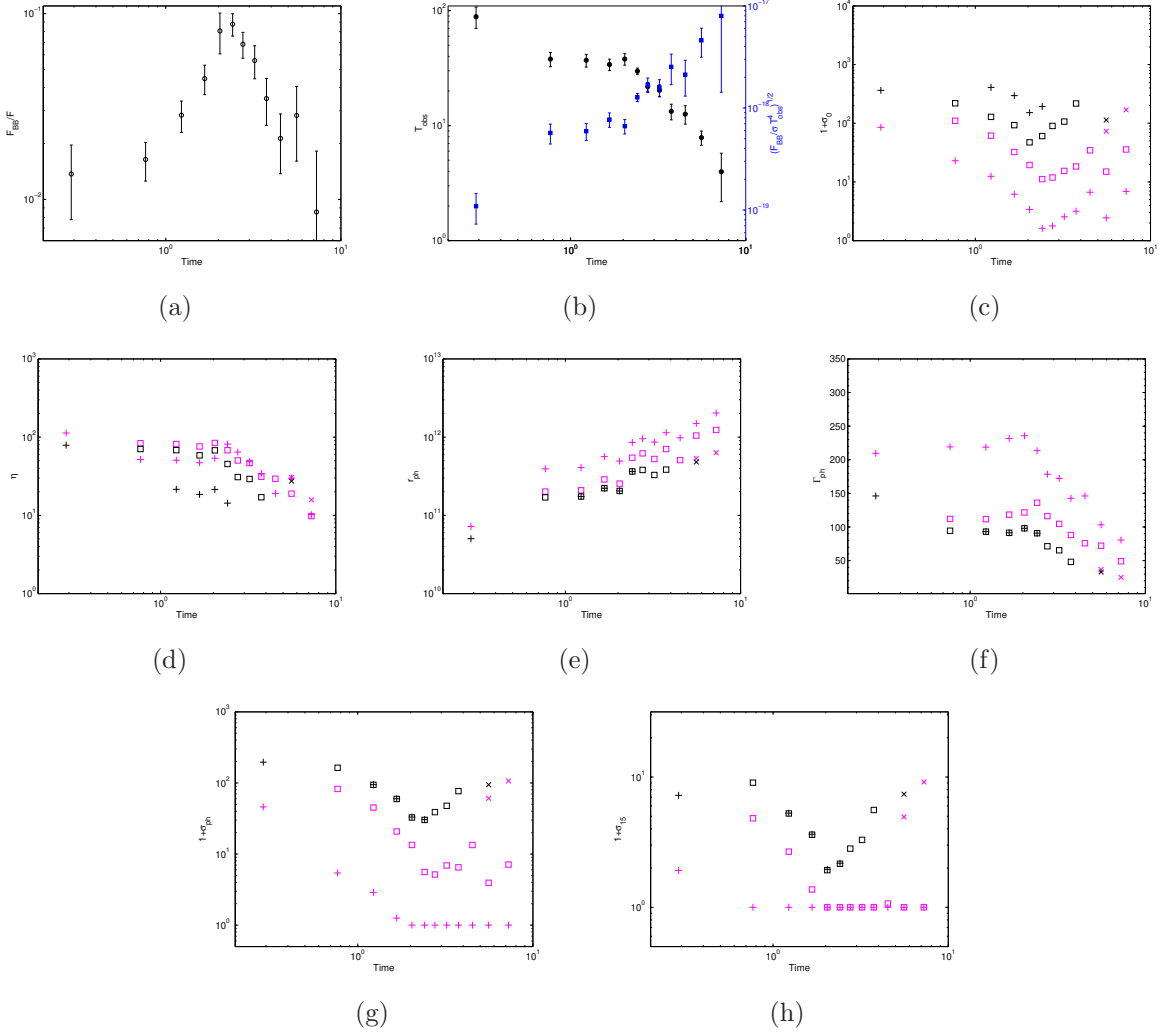


Fig. 5.— A case study for GRB 110721A. The observed $F_{\text{BB}}/F_{\text{ob}}$ (a) and the observed T_{BB} and $(F_{\text{BB}}/\sigma T_{\text{ob}}^4)^{1/2}$ (b) evolution (Iyyani et al. 2013), along with the derived parameters and their evolution: $1 + \sigma_0$ (c), η (d), r_{ph} (e), Γ_{ph} (f), $(1 + \sigma_{\text{ph}})$ (g), and $(1 + \sigma_{15})$ (h). The pink (black) symbols are for the cases of without (with) magnetic dissipation. The plus, square and cross symbols denote the cases with $r_0 = 10^8$ cm, 10^9 cm and 10^{10} cm, respectively.